ANNUAL REVIEWS

Annual Review of Fluid Mechanics

Turbulence with Large Thermal and Compositional Density Variations

Daniel Livescu

Computational Physics and Methods Group (CCS-2), Los Alamos National Laboratory, Los Alamos, New Mexico 87545, USA; email: livescu@lanl.gov

Annu. Rev. Fluid Mech. 2020. 52:309–41

First published as a Review in Advance on August 19, 2019

The *Annual Review of Fluid Mechanics* is online at fluid.annualreviews.org

https://doi.org/10.1146/annurev-fluid-010719-060114

Keywords

variable-density, Richtmyer–Meshkov, Rayleigh–Taylor, vertical convection, non-Oberbeck–Boussinesq, low–Mach number approximation

Abstract

Density variations in fluid flows can arise due to acoustic or thermal fluctuations, compositional changes during mixing of fluids with different molar masses, or phase inhomogeneities. In particular, thermal and compositional (with miscible fluids) density variations have many similarities, such as in how the flow interacts with a shock wave. Two limiting cases have been of particular interest: (*a*) the single-fluid non-Oberbeck–Boussinesq low–Mach number approximation for flows with temperature variations, which describes vertical convection, and (*b*) the incompressible limit of mixing between miscible fluids with different molar masses, which describes the Rayleigh–Taylor instability. The equations describing these cases are remarkably similar, with some differences in the molecular transport terms. In all cases, strong inertial effects lead to significant asymmetries of mixing, turbulence, and the shape of mixing layers. In addition, density variations require special attention in turbulence models to avoid viscous contamination of the large scales.

1. INTRODUCTION

Flow systems with large density variations are ubiquitous in technology and nature. Sources of variable-density (VD) effects include compressibility phenomena such as acoustic fluctuations and shock waves, temperature variations due to differential heating or chemical/nuclear reactions, mixing between fluids with different molar masses or phases, and phase transformations. At very large scales, all astrophysical explosions, accretion disks, and mergers, as well as convection in stars, involve turbulent flows with significant density variations. Detailed measurements of the flow characteristics under the most extreme conditions are not possible; only observations that are inherently limited in the timescales and phenomena they capture are available to inform numerical and theoretical models. At the opposite end of length- and timescale ranges are manmade implosions inside inertial confinement fusion (ICF) capsules at the National Ignition Facility. The implosions are measured in nanoseconds, and the capsules are only about a millimeter in diameter. While measurements are being performed for the flow within such capsules, the overlap of fluid [e.g., Richtmyer–Meshkov (RM), Rayleigh–Taylor (RT), ablative], laser beam, and plasma instabilities; phase changes; plasma and magnetic effects; and kinetic effects makes it extremely difficult to understand the flow. Between these limits, significant variations in fluid density are encountered in, for example, high-speed flight; combustion; convection regions in oceans, the atmosphere, and Earth's mantle; and industrial flows. Such a large variety of applications may seem overwhelming and all but impossible to understand. However, starting from conservation equations, one can identify canonical flows that exhibit aspects shared across applications. Designing canonical flows has facilitated the development of laboratory-sized experiments that expose relevant phenomena at widely different scales, such as in astrophysics or ICF (Prestridge 2018, Remington et al. 2019). These canonical flows have been studied in some cases for more than a century and have developed communities that have diverged as the fields grew.

The focus of this review is inertial density effects on turbulent flows, as produced by thermal (entropic) and compositional variations. These VD effects span several canonical turbulent flows in compressible flow regimes [e.g., RM instability (RMI)] and in low–Mach number (low-M) or incompressible flow regimes [e.g., RT instability (RTI), shear-driven mixing layers, vertical convection]. There are many similarities between thermal and compositional density variations, such as in how the flow interacts with a shock wave. Two limiting cases are the low-M approximation for single-fluid flows with thermal variations and the incompressible limit of binary mixing between different molar mass fluids, which are described by remarkably similar equations, with only subtle differences in the molecular transport terms. The former has been used to study non-Oberbeck–Boussinesq (NOB) effects in flows with the largest density variations at the boundaries (e.g., vertical convection), while the latter has been used to study flows with the largest density variations at an interior interface (e.g., RTI at large Atwood number A, where $A = \frac{\rho_2 - \rho_1}{\rho_2 + \rho_1}$ measures the normalized density difference), with some overlapping studies of shear-driven mixing layers. Due to the similarity of the governing equations, all of these flows share common features regarding asymmetric turbulence stirring and entrainment, while differences in the molecular transport may lead to changes in the dynamics of density gradients and higher-order quantities, affecting, for example, the evolution of pure fluid regions. Along the way, some of the mathematical aspects introduced by VD effects on the conservation equations are discussed. However, the goal is not to provide a comprehensive review of any of the flows mentioned, but rather to emphasize the shared VD effects. For particular details about each of these canonical flows, the reader is referred below to appropriate recent reviews.

This review is organized as follows. Section 2 starts from the fully compressible multispecies Navier–Stokes equations to first identify VD sources and the corresponding thermal (entropic)

and compositional effects. This is followed by a discussion of shock–VD flow interaction progressing from small-amplitude perturbations described by the linear interaction approximation (LIA) to shock propagation in a VD medium, shock–VD turbulence interaction, and finally, RMI. Section 3 discusses the derivation of the quasi-incompressible and incompressible limits of the compressible Navier–Stokes equations for VD flows. The derivation encompasses both thermal and compositional density variations to highlight their similarities and differences. This section also discusses VD effects in triply periodic simulations, regularity considerations for the limiting VD equations, and locality of the turbulence cascade in VD turbulence. Section 4 highlights manifestations of inertial density effects in several canonical turbulent flows: temporal shear-driven mixing layers, RTI, and thermal convection. The review ends with lists of summary points and future issues.

2. THERMAL (ENTROPIC) AND COMPOSITIONAL DENSITY VARIATIONS IN COMPRESSIBLE FLOWS

To isolate VD effects due to thermal (entropic) and compositional fluctuations from other sources, we assume the fluid is well described by the compressible multicomponent Navier–Stokes equations. The similarity and differences between thermal and compositional VD effects are studied in this section in the context of interaction with shock waves, and low-M limits are addressed in the subsequent sections.

2.1. Compressible Navier–Stokes Equations

In vector form, the governing equations describing the conservation of mass, momentum, energy, and species mass fractions for miscible materials are (Williams 1985)

$$\frac{\partial}{\partial t}\rho + \nabla\cdot(\rho\mathbf{u}) = 0, \tag{1.}$$

$$\frac{\partial}{\partial t}(\rho\mathbf{u}) + \nabla\cdot(\rho\mathbf{u}\mathbf{u}) = -\nabla\cdot\boldsymbol{\sigma} + \rho\sum_{\alpha} Y_\alpha\mathbf{F}_\alpha, \tag{2.}$$

$$\frac{\partial}{\partial t}(\rho e) + \nabla\cdot(\rho\mathbf{u}e) = -\boldsymbol{\sigma}:(\nabla\mathbf{u}) - \nabla\cdot\mathbf{q} + \dot{\Omega} + \rho\sum_{\alpha} Y_\alpha\mathbf{F}_\alpha\cdot\mathbf{V}_\alpha, \tag{3.}$$

$$\frac{\partial}{\partial t}(\rho Y_\alpha) + \nabla\cdot(\rho\mathbf{u}Y_\alpha) = -\nabla\cdot(\rho Y_\alpha\mathbf{V}_\alpha) + \dot{\omega}_\alpha. \tag{4.}$$

The primary dependent variables in Equations 1–4 are the mixture density ρ, mass-averaged velocity $\mathbf{u}$, specific internal energy e, and species mass fractions Y_α, with $\alpha = 1,\ldots,N$ and $\sum_\alpha Y_\alpha = 1$. The external body force, $\mathbf{F}_\alpha$, acting on species α is considered specified (not derived). Each species has its own velocity, which differs from the mixture velocity by the diffusional velocity, $\mathbf{V}_\alpha$, with $\sum_\alpha Y_\alpha\mathbf{V}_\alpha = 0$, and $\dot{\Omega}$ and $\dot{\omega}_\alpha$ are source terms due to chemical/nuclear reactions.

The molecular transport terms on the right-hand sides of Equations 1–4 represent transport of mass (the diffusional velocities, $\mathbf{V}_\alpha$), momentum (the stress tensor, $\boldsymbol{\sigma}$), and energy (the heat flux, $\mathbf{q}$). These quantities cannot, in general, be related to the primary variables, since the transport properties involve higher moments of the velocity distribution function. Neglecting radiative and Soret and Dufour effects, Chapman–Enskog theory leads to the following expressions for the

transport terms (Williams 1985),

$$\nabla X_\alpha = \sum_\beta \left(\frac{X_\alpha X_\beta}{D_{\alpha\beta}}\right)(\mathbf{V}_\beta - \mathbf{V}_\alpha) + (Y_\alpha - X_\alpha)\left(\frac{\nabla p}{p}\right) + \frac{\rho}{p}\sum_{\beta=1}^{N} Y_\alpha Y_\beta(\mathbf{F}_\alpha - \mathbf{F}_\beta), \quad 5.$$

$$\boldsymbol{\sigma} = p\mathbf{I} - \mu[\nabla\mathbf{u} + (\nabla\mathbf{u})^T] + \left(\frac{2}{3}\mu - \mu_b\right)\nabla\cdot\mathbf{u}\mathbf{I}, \quad 6.$$

$$\mathbf{q} = -\lambda\nabla T + \rho\sum_{\alpha=1}^{N} h_\alpha Y_\alpha \mathbf{V}_\alpha, \quad 7.$$

where W_α and X_α are respectively the molar mass and mole fraction of species α [$X_\alpha = (Y_\alpha/W_\alpha)/\sum_{\beta=1}^{N}(Y_\beta/W_\beta)$], p and T are the pressure and temperature of the mixture, $h_\alpha = \frac{\partial h}{\partial Y_\alpha}|_{p,T}$ is the enthalpy of species α, $\mathcal{R}$ is the universal gas constant, $\mathbf{I}$ is the unit second-order tensor, and $(\nabla\mathbf{u})^T$ denotes the matrix transpose of the velocity gradient. The equations need to be supplemented by pressure, $p = p(\rho, T, Y_\alpha)$, and energy, $e = e(\rho, T, Y_\alpha)$, equations of state.

2.2. Shock/Variable-Density Flow Interaction

The small-perturbation limit is briefly discussed first in order to identify VD sources in multicomponent compressible fluid flows, followed by discussions of shock propagation through VD media, shock interaction with isotropic VD turbulence, and finally, RMI.

2.2.1. Extended Kovasznay decomposition. For single-fluid flows with small density, velocity, pressure, and entropy variations around a background state, Kovasznay (1953) showed that the linearized Euler equations can be decomposed into three physical modes: vorticity, entropic, and acoustic. For multicomponent flows, there is also a compositional mode (Griffond 2005, Sagaut & Cambon 2018; Y. Tian, F.A. Jaberi & D. Livescu, manuscript in review). To highlight the contributions to the density variations from each of the modes, one can write the linearized continuity equation around a uniform background state denoted by index "0" in a reference frame moving with the mean velocity $\mathbf{u}_0$ in the form

$$\Delta \equiv \nabla\cdot\mathbf{u} = -\frac{1}{\rho_0}\frac{\partial\rho}{\partial t} = -\frac{1}{\gamma_0 p_0}\frac{\partial p}{\partial t} + \frac{1}{c_{p_0}}\frac{\partial s}{\partial t} + \sum_\alpha \frac{R_\alpha}{R_0}\frac{\partial Y_\alpha}{\partial t}, \quad 8.$$

for a mixture of perfect gases, obeying the equation of state $p = \rho RT$, with $R = \sum_\alpha \frac{\mathcal{R}}{W_\alpha}Y_\alpha = \sum_\alpha R_\alpha Y_\alpha$. Here, ρ, p, s, $\mathbf{u}$, and Y_α represent small fluctuations. It can be seen that the density and the dilatational part of the velocity have contributions from acoustic, entropic, and compositional modes. In the absence of sources and molecular transport, the modes decouple and the associated vorticity, entropy, and compositional disturbances are passively advected by the mean velocity, while the acoustic mode disturbances travel at the speed of sound relative to the mean flow.

2.2.2. Linear interaction approximation. For small-amplitude perturbations, the mode decomposition allows one to relate the perturbations downstream of the shock to those upstream using the linearized Rankine–Hugoniot jump relations (Moore 1954, Ribner 1954). For single-fluid flows, there have been numerous comparisons between experiments and simulations with the LIA, as well as further extensions (Andreopoulos et al. 2000). Of particular interest has been the interaction between a shock wave and isotropic turbulence. Ryu & Livescu (2014) showed

that the direct numerical simulations (DNS) results converge to the LIA solutions when the ratio of the shock thickness (δ) to the preshock Kolmogorov length scale (η_K) becomes small, even at low Reynolds numbers. In this limit, there is a large separation of scale between δ and turbulence scales, which also minimizes the interaction time and hence the role of viscous/diffusive contributions. Replacing the actual shock interaction with the LIA relations can extend the reach of DNS to arbitrarily high shock Mach number and much larger Taylor Reynolds number (Re_λ) than is otherwise computationally feasible, provided that the interaction parameters correspond to the linear regime (Livescu & Ryu 2016, Quadros et al. 2016). Using shock-capturing turbulence-resolving simulations, Tian et al. (2017) showed that the LIA predictions for the Reynolds stresses can be approached (albeit at larger Re_λ values than DNS calculations), provided that the scale separation between numerical shock thickness (δ_n) and η_K is large enough. Both shock-resolving and turbulence-resolving shock-capturing simulations have been used to study the postshock amplification of Reynolds stresses, vorticity variance, turbulence length scales, and terms in their transport equations (e.g., Mahesh et al. 1995, 1997, Jamme et al. 2002, Larsson et al. 2013, and references therein); passive scalar dynamics (Tian et al. 2017, Boukharfane et al. 2018); thermodynamic fields due to the interaction (Sethuraman et al. 2018); and improvements in turbulence modeling (Griffond et al. 2010, Schwarzkopf et al. 2016).

For a mixture of perfect gases, the linearized Rankine–Hugoniot jump conditions (e.g., Lee et al. 1993, Mahesh et al. 1995) should be supplemented with jump conditions for the composition variables, which simply become (Griffond 2005)

$$[\![Y_{\alpha_0}]\!] = 0, \quad [\![Y_\alpha]\!] = 0, \tag{9.}$$

showing that the composition wave is not changed through the shock wave. The resulting downstream perturbations can be written as solutions to the linear system $\mathbf{A} \cdot \mathbf{Z}_l = B_l$, where the transfer function $\mathbf{Z}_l = (Z_{lv}, Z_{ls}, Z_{la}, Z_{lc}, Z_{lx})$ measures the relative amplitude of the created perturbations to the incident perturbation. The first subscript denotes the kind of incident wave, and the second the kind of created perturbation (v for vorticity, s for entropy, a for acoustic, c for composition, and x for shock front deformation) (Griffond 2005). Any type of incident perturbation generates all other types behind the shock; however, Equation 9 implies that Z_{cc} equals 1. Therefore, the corresponding cc entries can be removed from matrix $\mathbf{A}$. The remaining matrix is the same as the single-fluid matrix for the mixture (Griffond 2005, Griffond & Soulard 2012). Thus, in the absence of viscous and diffusive effects, for small-amplitude perturbations, density fluctuations generated by thermal (entropic) or compositional density variations produce identical effects on vorticity and acoustic modes or shock deformation. Of course, the entropic and compositional waves themselves respond differently to the interaction with the shock wave. For an upstream multimode density field, the downstream fluctuations can be integrated to form closed Reynolds stresses solutions, irrespective of the source of density fluctuations, thermal or compositional (de Lira et al. 2011, Griffond & Soulard 2012). The similarities and differences between thermal and compositional density fluctuations are further explored in the next sections.

2.2.3. Shock propagation in a variable-density medium. The analogy between flows with thermal and compositional density variations interacting with shock waves can be extended to larger A, provided that viscous and diffusive effects remain negligible. For a shock wave propagating through a nonuniform density medium, the strength and geometry of the shock wave, as well as the medium itself, are modified through their interactions. However, assuming that the density profile can be decomposed into a large number of uniform regions separated by weak discontinuities, Chisnell (1955) and Whitham (1958) were able to develop an analytical model for the

one-dimensional (1D) shock propagation. Using the method of characteristics, Bird (1961) showed that the rereflected waves are important for the shock propagation in a linearly decreasing density field. The results are in good agreement with experimental studies (Hesselink & Sturtevant 1988) for a weak shock propagation through a random medium. Soukhomlinov et al. (2002) further examined the effects of temperature gradients on shock propagation, matching the results of Bird (1961). For a fluctuating 1D density profile, the rereflected waves play an even more important role (Tian et al. 2019b). Nevertheless, so long as there is a large-scale separation between the density variations and δ, there is an equivalence between upstream thermal (entropic) and compositional density fluctuations. Thus, for the Shu–Osher problem, where the density varies sinusoidally, density and pressure variations behind the shock are identical for the two cases (Y. Tian, F.A. Jaberi & D. Livescu, manuscript in review), while the temperature fluctuations themselves are different.

2.2.4. Shock/variable-density turbulence interaction. The current analytical models become intractable for shock propagation through media with large 3D density variations. Numerical results (Tian et al. 2019b; Y. Tian, F.A. Jaberi & D. Livescu, manuscript in review) have revealed the complex role of the rereflected waves and also the nonlinear response to density field anisotropy. When the upstream flow is turbulent, the presence of large density variations profoundly changes the downstream turbulence structure. The canonical shock–isotropic turbulence interaction setup can be extended to include thermal or compositional density variations in the upstream turbulence. By adjusting the outflow pressure (Larsson & Lele 2009), one makes the problem quasi-stationary in the reference frame moving with the nominal shock speed, representing a statistically stationary version of RMI.

When a shock wave interacts with VD isotropic turbulence, turbulence amplification is much higher and the reduction in turbulence length scales is more significant, due to the modifications in the local shock strength (Tian et al. 2017). As turbulence evolves away from the shock, enhanced turbulent stirring in turn increases molecular mixing. This results in a mixing asymmetry in the postshock region (**Figure 1**). Turbulent statistics also acquire a differential distribution in regions having different densities subsequent to the interaction with the shock. The various manifestations

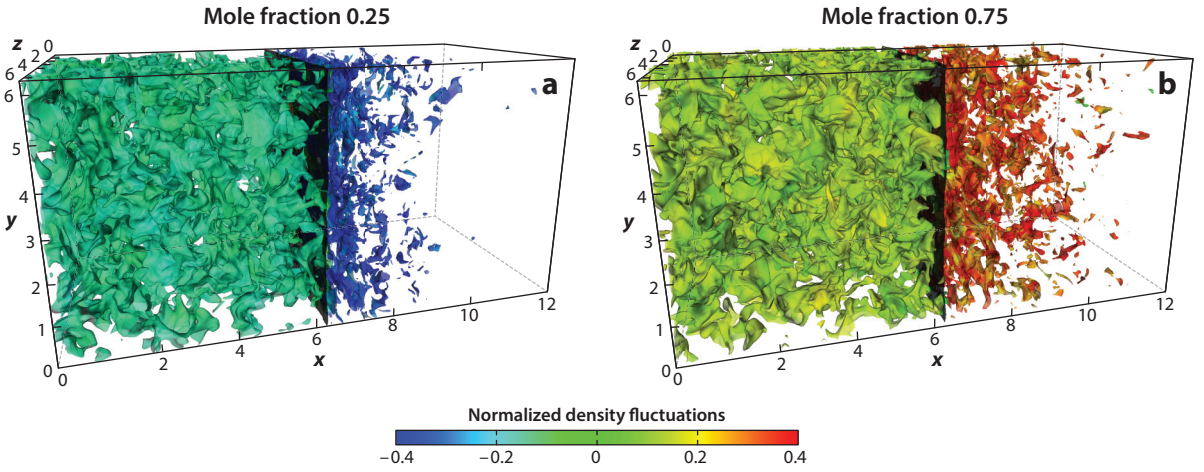

Figure 1

Scalar structure in variable-density turbulence interacting with a Mach 2 shock identified by the isosurface of heavy-fluid mole fraction and colored by the instantaneous density fluctuations normalized by the mean density. The black plane represents the instantaneous shock surface. Figure adapted with permission from Tian et al. (2017).

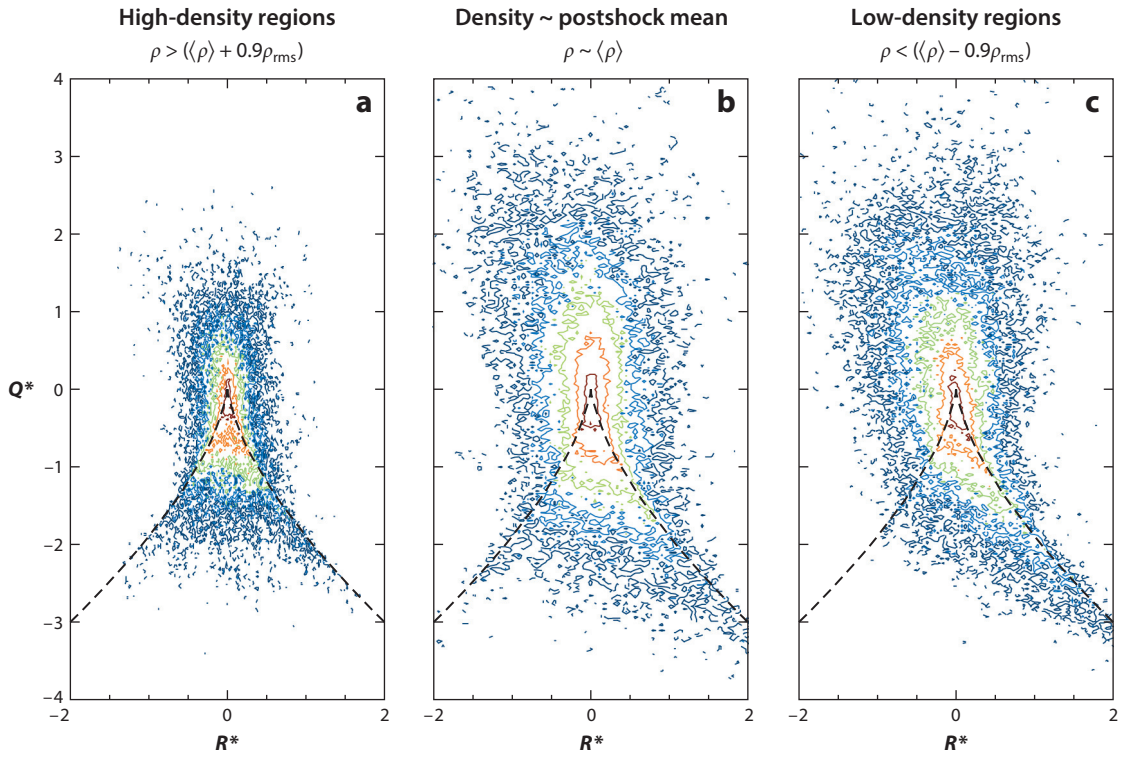

Figure 2

Isocontour lines of the postshock ($k_0 x \approx 0.44$, where k_0 is the wave number corresponding to the peak of the incoming turbulence kinetic energy spectrum) joint probability density function of the second and third invariants of the anisotropic part of the velocity gradient tensor, Q^* and R^*, respectively, in (*a*) high-density regions, (*b*) regions with density around the postshock mean value $\langle\rho\rangle$, and (*c*) low-density regions. Figure adapted with permission from Tian et al. (2019a).

of these largely inertial effects (light-fluid regions respond faster to acceleration and changes in the local strain than heavy-fluid regions) coupled with the corresponding modifications in scalar (mass fraction or temperature) variance dissipation are shown below to be features of all canonical flow examples discussed is this review.

Compared to the single-fluid case, density variations significantly change the turbulence structure and flow topology. Thus, in the postshock flow for the multifluid case, the correlation between rotation and strain is weaker, while one observes a stronger symmetrization of the joint probability density function (PDF), $\mathcal{P}(Q^*, R^*)$, of the second and third invariants of the anisotropic velocity gradient tensor, as well as of the PDF of the vortex stretching contribution to the enstrophy equation (Tian et al. 2019a). A short distance after the shock, the light-fluid regions recover the 3D turbulence structure, while the heavy-fluid regions remain quasi-2D due to different timescales for the response to changes in the local strain. Thus, after conditioning $\mathcal{P}(Q^*, R^*)$ based on fluid density, **Figure 2** shows that the joint PDF is almost completely symmetrical in the heavy-fluid regions, with a large portion of data in the third quadrant. In contrast, most of the light-fluid data points have a distribution similar to that of isotropic turbulence.

Numerical simulations with small upstream thermal density variations matching those found in boundary layers (Mahesh et al. 1997) are consistent with the enhanced turbulence amplification through the shock discussed above. While the shock–turbulence interaction has not

been explored for flows with large thermal density variations, when the shock thickness is much smaller than the density length scales, presumably the equivalence with compositional density variations is carried over. Nevertheless, turbulence response downstream of the shock may be different.

2.2.5. Richtmyer–Meshkov instability. RMI is a fundamental hydrodynamic flow instability that occurs when a shock wave passes through a material interface between fluids of different densities (Zabusky 1999; Brouillette 2002; Zhou 2017a,b). The instability is initiated by the deposition of vorticity at the interface due to the misalignment between pressure and density gradients across the shock wave and material interface. RMI plays an important role in the dynamics of supernovae and other astrophysical explosions (Almgren et al. 2006a), mixing enhancement in supersonic/hypersonic combustion (Khokhlov et al. 1999), and ICF (Aglitskiy et al. 2014).

After the passage of the shock, the flow is essentially decaying incompressible VD turbulence (Poggi et al. 1998, Wong et al. 2019). Therefore, the growth of the mixing region is largely dependent on the characteristics of the initial perturbation (Thornber et al. 2010), and hence a precise control of the initial conditions is required in experiments (Balakumar et al. 2012; Balasubramanian et al. 2012; Weber et al. 2013, 2014; Orlicz et al. 2015; Mohaghar et al. 2017; Reese et al. 2018). If the Reynolds number is sufficiently high, small-scale turbulent features develop beyond the mixing transition when a further increase of the Reynolds number (i.e., the range of scales) does not yield significant changes in the turbulence characteristics (Dimotakis 2000, Cook et al. 2004). The transition to turbulence occurs faster if the mixing layer is subjected to an additional shock wave interaction, i.e., reshock (e.g., Hill et al. 2006, Lombardini et al. 2012, Tritschler et al. 2014b), which is relevant to the ICF application. Further relevance to the ICF application is obtained using spherical interfaces (Lombardini et al. 2014a,b).

Due to the moving shock, the resolution requirements for shock-resolving DNS-like simulations, with enough realizations for statistical convergence, are out of reach for today's computers. Similarly, experiments with controlled initial conditions and measurements of higher-order turbulence statistics are extremely difficult. Therefore, as opposed to the stationary shock–turbulence interaction problem, data regarding the higher-order turbulence structure are scarce. In addition, similar to the classical turbulence decay problem, the decay law and subsequent mixing layer growth are strongly dependent on the lowest frequencies in the turbulent kinetic energy (TKE) spectrum (Tritschler et al. 2014a) and require extremely large cross-sections for a well-established low–wave number spectrum. For finite layer widths, the growth of the layer width, h, is well approximated by a power law of the form $h - h_0 = (t - t_0)^n$ (Weber et al. 2013), with the subscript "0" indicating the virtual origin. When a reshock is present, h_0 and t_0 correspond to the layer width and time at reshock, respectively (Wong et al. 2019). Values between 0.48 and 0.63 have been reported for n in 2D (Thornber & Zhou 2015, Wong et al. 2019) and between 0.25 and 0.3 in 3D, with an intermediate stage where n is around 0.4 (Thornber et al. 2011, Tritschler et al. 2014a, Wong et al. 2019). Similarly, the decay of TKE follows a power law of the form $\mathrm{TKE} = (t - t_0)^{-m}$ (Tritschler et al. 2014a). Exponent m values around 0.5 in 2D and 10/7 in 3D have been reported (Lombardini et al. 2012, Tritschler et al. 2014a, Wong et al. 2019), indicating a Batchelor-type decay. In contrast, global statistics like mixedness (Youngs 1994),

$$\Theta = \frac{\int \langle X_\mathrm{H}\,(1 - X_\mathrm{H})\rangle \,\mathrm{d}x}{\int \langle X_\mathrm{H}\rangle \langle 1 - X_\mathrm{H}\rangle \,\mathrm{d}x},$$

where X_H is the mole fraction of the heavy fluid, asymptote to similar values (~0.85) among experiments (e.g., Tomkins et al. 2008; Weber et al. 2013, 2014) and simulations (e.g., Lombardini et al. 2012, Tritschler et al. 2014a, Thornber et al. 2017, Wong et al. 2019). Other global statistics to describe the mixing state have also been proposed that are more sensitive to the Atwood number (Zhou et al. 2016).

The sign of the Atwood number A plays an important role in determining the mechanism by which additional TKE is deposited after reshock. Thus, in the light–heavy cases, there is more turbulent activity following the first expansion–wave interaction than occurs after the secondary reshocks in the heavy–light configuration (Lombardini et al. 2011). As the density ratio increases, the mixing layer grows asymmetrically (**Figure 3**), with more elongated structures on the light-fluid side (i.e., spikes) and more rounded structures on the heavy-fluid side (i.e., bubbles) (Lombardini et al. 2011, Wong et al. 2019). At the same time, the layer center based on the 50% heavy-fluid mole fraction moves off the initial centerline, based on the sign of A. This asymmetry is present in all canonical VD flows surveyed here and is discussed in more detail below.

3. INCOMPRESSIBLE AND QUASI-INCOMPRESSIBLE LIMITS

A broad range of flows with large density variations occurs in low-M regimes, when the fluid velocity is much less than the speed of sound. Such flows can be well described by the Navier–Stokes equations after the acoustic waves are filtered out (Majda & Sethian 1985, Chenoweth & Paolucci 1986, Day & Bell 2000). In this section, we discuss the derivation of these equations, their general characteristics, triply periodic simulations, regularity considerations, and locality of the turbulence cascade for VD turbulence.

3.1. Low–Mach Number Approximation for Flows with Thermal and Compositional Variations

To keep the derivation general to include both thermal and compositional variations, we follow Day & Bell (2000) and Almgren et al. (2006a) and start from rewriting the energy transport equation as a transport equation for the enthalpy, $h = e + p/\rho$, i.e.,

$$\rho \frac{\mathrm{D}h}{\mathrm{D}t} = \frac{\mathrm{D}p}{\mathrm{D}t} - \nabla \cdot \mathbf{q} + \Phi + B + \dot{Q}, \tag{10.}$$

where $\frac{\mathrm{D}}{\mathrm{D}t} = \frac{\partial}{\partial t} + \mathbf{u} \cdot \nabla$ is the material derivative and $\Phi = -\boldsymbol{\sigma} : (\nabla \mathbf{u})$ and $B = \rho \sum_\alpha Y_\alpha \mathbf{F}_\alpha \cdot \mathbf{V}_\alpha$ are the viscous and buoyancy contributions, respectively. Then, after taking the material derivatives of the pressure, $p = p(\rho, T, Y_\alpha)$, and caloric, $h = h(p, T, Y_\alpha)$, equations of state, one can find an expression for the material derivative of the density. Given $\nabla \cdot \mathbf{u} = -\frac{1}{\rho}\frac{\mathrm{D}\rho}{\mathrm{D}t}$, the velocity divergence can then be written as

$$\nabla \cdot \mathbf{u} = -\frac{1}{\rho p_\rho}\left\{\frac{\mathrm{D}p}{\mathrm{D}t}\left[1 - \frac{p_T}{\rho c_p}\left(1 - \rho h_p\right)\right] + \frac{p_T}{\rho c_p}\left[\rho \sum_\alpha h_\alpha \frac{\mathrm{D}Y_\alpha}{\mathrm{D}t} + \nabla \cdot \mathbf{q} - \Phi - \mathbf{B} - \dot{Q}\right] - \sum_\alpha p_\alpha \frac{\mathrm{D}Y_\alpha}{\mathrm{D}t}\right\}, \tag{11.}$$

where the thermodynamic partial derivatives are denoted as $p_\rho = \frac{\partial p}{\partial \rho}|_{T,Y_\alpha}$, $p_T = \frac{\partial p}{\partial T}|_{\rho,Y_\alpha}$, $p_\alpha = \frac{\partial p}{\partial Y_\alpha}|_{\rho,T}$, $h_p = \frac{\partial h}{\partial p}|_{T,Y_\alpha}$, $c_p = \frac{\partial h}{\partial T}|_{p,Y_\alpha}$, and $h_\alpha = \frac{\partial h}{\partial Y_\alpha}|_{p,T}$, with c_p the specific heat at constant pressure. The material derivative of the mass fraction can be extracted from Equation 4.

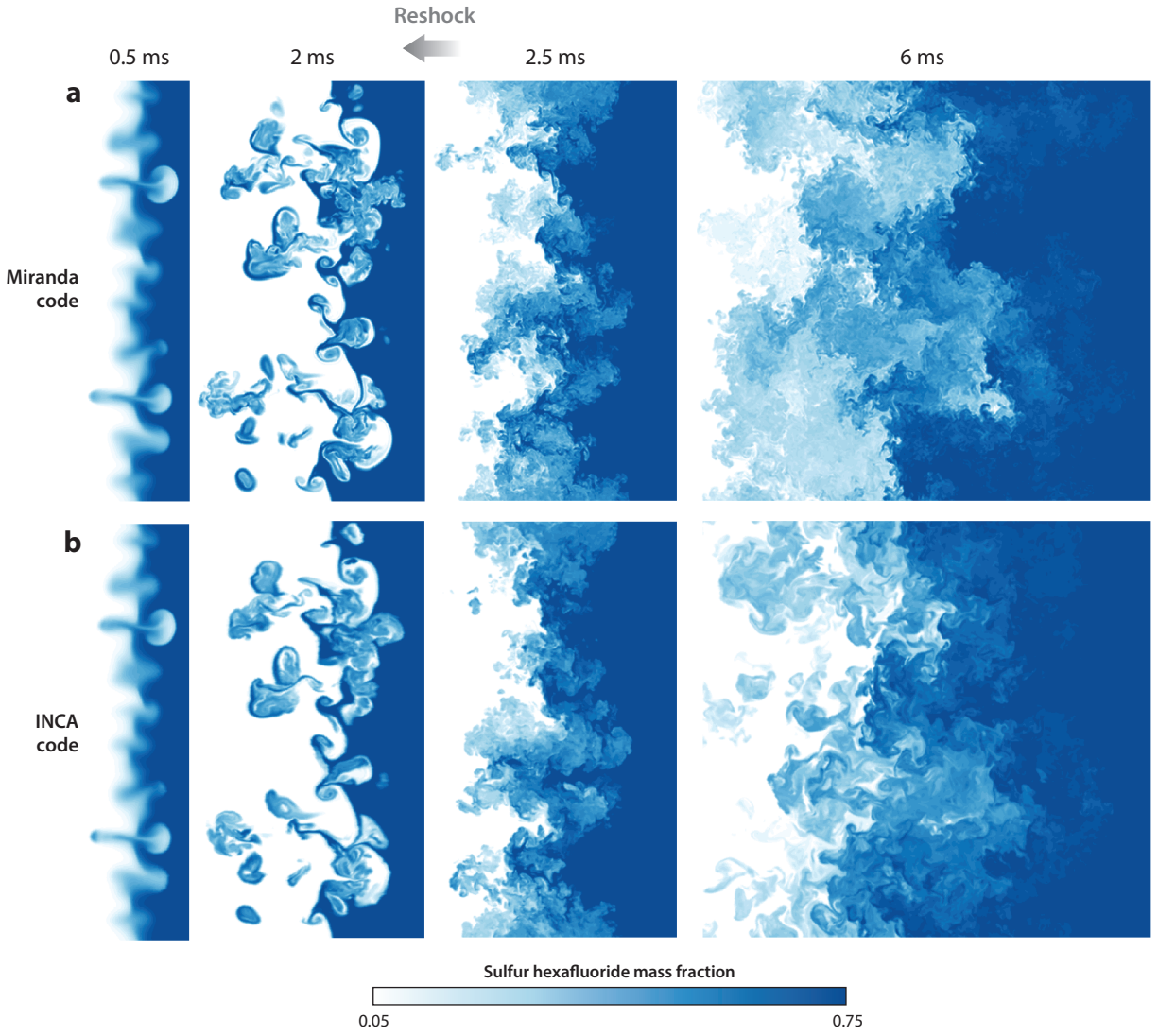

Figure 3

Sulfur hexafluoride mass fraction evolution in Richtmyer–Meshkov instability with reshock for Atwood number $A \approx 0.68$ from (*a*) Miranda and (*b*) INCA codes. The contours range from 0.05 (*white*) to 0.75 (*blue*). Figure adapted with permission from Tritschler et al. (2014a).

For low-M flows, the pressure can be expanded as $p \approx p_0 + \pi$, where π is the order of the Mach number squared ($\pi \sim M^2 p_0$) (Majda & Sethian 1985). Then, p_0 is the thermodynamic component and π is the dynamic component appearing in the momentum equations. Since large density variations can appear due to thermal or compositional changes without affecting the background pressure, for such flows, density and temperature expansions in terms of M are not justified. For domains large enough that background stratification cannot be neglected, for example, in stellar interiors (Almgren et al. 2006a), p_0 can retain time-independent spatial variation in certain directions. However, in most other applications, p_0 is approximated as spatially

constant (Rehm & Baum 1978, Chenoweth & Paolucci 1986, McMurtry et al. 1986, Pember et al. 1998, Nicoud 2000). After replacing $\frac{Dp}{Dt}$ with $\frac{dp_0}{dt}$, Equation 11 gives the velocity divergence for a general fluid in the low-M approximation. It includes both thermal effects, through the divergence of the heat flux, $\nabla \cdot \mathbf{q}$, and compositional effects, through $\frac{DY_\alpha}{Dt}$ and $\nabla \cdot \mathbf{q}$. Thus, in general, nonzero divergence of velocity can be generated in the presence of background pressure changes, heat conduction, viscous dissipation, differential buoyancy forces, heat release, reactions between species with different molar masses, and mass diffusion.

Using the low-M approximation in the momentum equations results in

$$\frac{\partial}{\partial t}(\rho \mathbf{u}) + \nabla \cdot (\rho \mathbf{u}\mathbf{u}) = -\nabla \pi + \nabla \cdot \tau + \rho \sum_{\alpha=1}^{N} Y_\alpha \mathbf{F}_\alpha, \qquad 12.$$

while the continuity Equation 1 does not change compared to the fully compressible case. Here τ is the viscous stress tensor.

Almgren et al. (2006a,b), Zingale et al. (2009, 2015), and Gilet et al. (2013) have used Equations 1, 4, and 10–12, with stellar equations of state, to calculate the flow in type Ia supernovae, convection in stars, and type I X-ray bursts using the MAESTRO code (Nonaka et al. 2010). For these simulations, to close the system, the spatial variation of p_0 is specified or $\frac{dp_0}{dt}$ is set to zero. In addition, viscous dissipation was neglected in Equation 10, as were the diffusive effects in Equation 4.

For a mixture of ideal gases, the equations of state in the VD low-M approximation are $p_0 = \rho RT$ and $h = \sum_\alpha Y_\alpha h_\alpha(T)$. Then we have $p_T = \rho R$, $p_\rho = RT$, and $h_p = 0$. For $\mathbf{F}_\alpha = \mathbf{g}$, Equation 11 becomes

$$\nabla \cdot \mathbf{u} = -\frac{1}{\gamma p_0}\frac{dp_0}{dt} + \frac{R}{c_p p_0}\left[-\sum_\alpha (\rho Y_\alpha \mathbf{V}_\alpha)\cdot \nabla h_\alpha + \nabla \cdot (\lambda \nabla T) + \Phi\right]$$
$$-\frac{1}{\rho R}\sum_\alpha \nabla \cdot (\rho Y_\alpha \mathbf{V}_\alpha R_\alpha) + \frac{1}{\rho}\left[\frac{\rho R}{c_p p_0}\dot{Q} + \sum_\alpha \left(\frac{R_\alpha}{R} - \frac{h_\alpha}{c_p T}\right)\dot{\omega}_\alpha\right]. \qquad 13.$$

Several authors have used various simplifications of the system of Equations 1, 4, 10, 12, and 13 to study heat release effects in low-speed flows (e.g., McMurtry et al. 1986, Givi 1989, Pember et al. 1998, Day & Bell 2000). The effects of viscous dissipation have generally been neglected in Equation 13. In most of these studies, the contribution from $\frac{dp_0}{dt}$ was set to zero. This is justified in an open domain, where it can be argued that the background pressure equilibrates to the ambient pressure. For a closed system with adiabatic walls, McMurtry et al. (1986) calculated $\frac{dp_0}{dt}$ by integrating Equation 13, without the mass diffusion and species source terms, as given by the total heat release within the domain. Day & Bell (2000) considered the effects of heat conduction, Fickian mass diffusion, and species source terms to calculate laminar diffusion flames with complex chemistry. More recent applications of the equations to reacting flow calculations include Safta et al. (2010), Motheau & Abraham (2016), and references therein.

Below, the low-M equations are further simplified for nonreacting flows, where the velocity divergence is nonzero due to heat conduction or mass diffusion effects.

3.1.1. Low–Mach number approximation for single-fluid flows with temperature variations. For single-fluid flows without heat release, neglecting Φ, Equation 13 becomes

$$\nabla \cdot \mathbf{u} = -\frac{1}{\gamma p_0}\frac{dp_0}{dt} + \frac{R}{c_p p_0}\nabla \cdot (\lambda \nabla T). \qquad 14.$$

For a closed cavity with constant temperature walls, as encountered in thermal convection problems (Chenoweth & Paolucci 1986, Wang et al. 2019), p_0 can be determined by integrating the equation of state,

$$p_0 = \frac{RM_0}{\int_V \frac{1}{T}\,\mathrm{d}V}, \tag{15.}$$

as the mass of the system, $M_0 = \int_V \rho\,\mathrm{d}V$, is constant. In this case, the energy equation is retained as

$$\rho c_p \frac{\mathrm{D}T}{\mathrm{D}t} = \frac{\mathrm{d}p_0}{\mathrm{d}t} + \nabla\cdot(\lambda\nabla T). \tag{16.}$$

When the material properties c_p, λ, and μ retain their temperature dependence, the system of Equations 1, 12, and 14–16, together with the equation of state $p_0 = \rho RT$, includes most of the NOB effects (Wang et al. 2019), i.e., those effects neglected in the Oberbeck–Boussinesq (OB) approximation (Rajagopal et al. 1996). Additional sources of NOB effects could be due to background stratification and compressibility effects. Unless the background stratification remains approximately constant (for example, in stably stratified flow problems), both of these effects require the solution of the fully compressible flow equations. The high-A RTI discussed in Section 4.2 is an example of a case where the change in the background stratification prevents the use of the single-fluid low-M approximation. For this flow, the incompressible limit discussed in Section 3.2 is a useful approximation.

In nondimensional form, Equations 1, 12, and 14–16 are

$$\frac{\partial}{\partial t}\rho + \nabla\cdot(\rho\mathbf{u}) = 0, \tag{17.}$$

$$\frac{\partial}{\partial t}(\rho\mathbf{u}) + \nabla\cdot(\rho\mathbf{u}\mathbf{u}) = -\nabla\pi + \frac{1}{Re}\nabla\cdot\tau + \frac{1}{Fr^2}\rho\mathbf{g}, \tag{18.}$$

$$\nabla\cdot\mathbf{u} = \frac{1}{c_p p_0}\left[\left(\Gamma - c_p\right)\frac{\mathrm{d}p_0}{\mathrm{d}t} + \frac{1}{RePr}\nabla\cdot(\lambda\nabla T)\right], \tag{19.}$$

$$p_0 = \frac{M_0}{\int_V \frac{1}{T}\,\mathrm{d}V}, \tag{20.}$$

$$\rho c_p \frac{\mathrm{D}T}{\mathrm{D}t} = \Gamma\frac{\mathrm{d}p_0}{\mathrm{d}t} + \frac{1}{RePr}\nabla(\lambda\nabla T), \tag{21.}$$

$$p_0 = \rho T, \tag{22.}$$

where dimensional reference scales for length (L), velocity (u_∞), time ($t_\infty = L/u_\infty$), density (ρ_∞), temperature (T_∞), body force (g_∞), specific heat at constant pressure [$c_{p_\infty} = c_p(T_\infty) = \frac{R\gamma_\infty}{\gamma_\infty - 1}$], dynamic viscosity [$\mu_\infty = \mu(T_\infty)$], and heat conduction coefficient [$\lambda_\infty = \lambda(T_\infty)$] have been used to nondimensionalize the equations. Then the background pressure is nondimensionalized by $R\rho_\infty T_\infty$, the dynamic pressure by $\rho_\infty u_\infty^2$, volume by L^3, and the system mass by $\rho_\infty L^3$, and the nondimensional parameters appearing in Equations 17–22 are the Reynolds number (Re), Prandtl number (Pr), Froude number (Fr), and Γ, defined by

$$Re = \frac{\rho_\infty u_\infty L}{\mu_\infty}, \quad Pr = \frac{\mu_\infty c_{p_\infty}}{\lambda_\infty}, \quad Fr^2 = \frac{u_\infty^2}{g_\infty L}, \quad \Gamma = \frac{R}{c_{p_\infty}} = \frac{\gamma_\infty - 1}{\gamma_\infty}. \tag{23.}$$

For simplicity, the same notations have been used for the nondimensional primary variables (ρ, $\mathbf{u}$, T, and p_0) and dependent variables (length and time), as well as the body force, $\mathbf{g}$. In deriving the coefficient of $\frac{dp_0}{dt}$ in Equation 19, the dimensional ideal gas thermodynamic relation $R - c_p = -\frac{c_p}{\gamma}$ has been used. The normalized viscous stress tensor follows the Newtonian and Stokes assumptions, $\boldsymbol{\tau} = \mu[\nabla\mathbf{u} + (\nabla\mathbf{u})^T + \frac{2}{3}\nabla\cdot\mathbf{u}\mathbf{I}]$.

In convection problems, it is useful to introduce the normalized temperature difference $\epsilon = \Delta T/(2T_\infty)$ in the nondimensional expressions, where ΔT is the temperature difference between the hot and cold boundaries. Then the velocity scale is chosen as $\sqrt{2\epsilon g_\infty L}$. For nonideal fluids, the coefficient of volume expansion, $\beta = -\frac{1}{\rho}\frac{\partial\rho}{\partial T}|_{p,Y_\alpha} = \frac{p_T}{\rho p_\rho}$, also appears in the nondimensional parameters, as inferred from Equation 11. For ideal gases, β equals $\frac{1}{T}$. In this scaling, the Froude number no longer appears in the equations. The factors $1/Re$ and $1/Fr^2$ are replaced by $\sqrt{Pr/Ra} = 1/\sqrt{Gr}$ and $1/(2\epsilon)$, respectively, in the momentum Equation 18, and $1/(Re\,Pr)$ is replaced by $1/\sqrt{RaPr} = 1/(Pr\sqrt{Gr})$ in front of the conduction term in Equations 19 and 21. The Rayleigh number is defined as

$$Ra = \frac{2\epsilon T_\infty \beta_\infty \rho_\infty^2 c_{p\infty} g L^3}{\mu_\infty \lambda_\infty}, \qquad 24.$$

and the Grashof number is $Gr = Ra/Pr$. In this case, the Richardson number, $Ri = Gr/Re^2$, defines the importance of forced versus free convection.

The system of Equations 17–22 is overdetermined. In practice, either one uses only one of Equations 17 and 21, with the remaining variable found from the Equation of State 22, or one uses both Equations 17 and 21 for an additional numerical constraint (Majda & Sethian 1985, Day & Bell 2000, Nicoud 2000). In thermal convection problems, usually c_p equals 1, and the dimensionless conduction and viscosity coefficients are given by Sutherland laws,

$$\lambda = T^{1.5}\frac{1+S_\lambda}{T+S_\lambda} \quad \text{and} \quad \mu = T^{1.5}\frac{1+S_\mu}{T+S_\mu}, \qquad 25.$$

respectively, where the values of S_λ and S_μ depend on the fluid. The low-M Equations 17–22, together with material property relations in Equation 25 [hereafter, the low-M NOB (LMNOB) equations], have been used to estimate NOB effects in vertical convection (Section 4.3).

For periodic boundary conditions or bounded domains with adiabatic walls, if c_p equals 1, integration of Equation 19 shows that $\frac{dp_0}{dt}$ is zero. The background pressure is also constant for open boundaries. Then, the nondimensional temperature can be determined from the equation of state, $T = \frac{1}{\rho}$. In this case, the divergence of velocity becomes simply

$$\nabla\cdot\mathbf{u} = \frac{1}{RePr}\nabla^2\left(\frac{1}{\rho}\right). \qquad 26.$$

Equations 17, 18, and 26 have been used to calculate horizontal mixing in an external acceleration field (Gat et al. 2017) (Section 3.4) and shear-driven turbulence between two streams of different temperatures at high A (Almagro et al. 2017) (Section 4.1).

3.2. Incompressible Limit of Miscible Multifluid Flows

So far, the background pressure, p_0, has been assumed to be finite, even though it is large compared to the dynamic pressure contribution. One can further consider the fully incompressible case when the speed of sound, c, is infinite (i.e., $c \to \infty$). Since the compressible to incompressible limit is not generally unique (Livescu 2013), it is assumed that the incompressible limit is

reached by changing the background thermodynamic conditions and that the fluid model remains valid even for infinite c. For a mixture of ideal gases, this means that T is infinite, since c^2 equals γRT, and from the equation of state, that p_0 is infinite, since ρ is greater than zero. The second condition implies that the flow fluctuations remain finite, so that the baro-diffusion term, which is proportional to $\nabla p/p_0$, vanishes in the multicomponent diffusion operator of Equation 5 and the first square parenthesis vanishes in the velocity divergence Equation 13. The same condition implies that the temperature dependencies of the material properties γ, μ, λ, and $\mathcal{D}$ become functions of the background temperature state only. They may still retain spatial variations through density fluctuations, however. Furthermore, since the fluctuations within the flow are finite, the equation of state, $P_0/T = \rho R$, yields that ρR is uniform throughout the domain, so that we have

$$\rho = \frac{1}{\sum_\alpha \frac{Y}{\rho_\alpha}}, \tag{27.}$$

where the microdensities of the fluids, defined by $\rho_\alpha = \frac{W_\alpha p}{\mathcal{R}T}$, are constant in space. Since finite fluctuations cannot lead to infinitely large changes in p_0, Equation 13 shows that $\frac{\mathrm{d}p_0}{\mathrm{d}t}$ is zero, which implies that ρR and ρ_α are also constant in time. In terms of the thermal convection nondimensionalization from Section 3.1.1, the importance of thermal conduction versus mass diffusion is given by the scaled Richardson number, $Ri^\dagger = \frac{GrSc}{Re^2 Pr}$. For $Ri^\dagger \ll 1$, heat conduction drops from the expression for the divergence of velocity.

If the species equations contain reaction source terms, these terms generally do not vanish from Equation 13. For nonreacting materials, the velocity divergence then becomes

$$\nabla \cdot \mathbf{u} = -\frac{1}{\rho R} \sum_\alpha \nabla \cdot (\rho Y_\alpha \mathbf{V}_\alpha R_\alpha). \tag{28.}$$

Finally, to close the system, one needs to use Maxwell's relations (Williams 1985) to solve for the diffusion velocities. The derivation above can be generalized to nonideal fluids by using Equation 11 and noticing that, under the same assumptions, $c \to \infty$ leads to $p_\rho \to \infty$, while p_T should remain finite. In practice, the values of p_0 and T for which the flow is close to incompressible differ from substance to substance. For example, the incompressible assumption is a good approximation for mixing of water and brine at standard conditions. In this case, Equation 27 can be derived by assuming that the microdensities of the fluids are constant, such that the volume occupied by the mixture is equal to the volume occupied by the unmixed constituents at their respective microdensities (Joseph 1990, Cook & Dimotakis 2001, Livescu & Ristorcelli 2007), without invoking the ideal-gas equation of state. Substituting this equation into the species transport equation leads to Equation 28. The same relation is found from the energy equation (Livescu 2013), as required for consistency.

3.2.1. Binary case. If the diffusion coefficients are all the same or in the binary case, the divergence of velocity reduces to $\nabla \cdot \mathbf{u} = -\nabla \cdot [\mathcal{D}\nabla (\ln \rho)]$. In nondimensional form, when the diffusion coefficient is not a function of density, the velocity divergence becomes

$$\nabla \cdot \mathbf{u} = -\frac{1}{ReSc} \nabla^2 (\ln \rho), \tag{29.}$$

where the Schmidt number is defined by $Sc = \frac{\mu_\infty}{\rho_\infty \mathcal{D}}$. The viscosity variation in Equation 18 is no longer described by a Sutherland-type relation. To ensure a uniform Sc throughout the flow, studies using these equations usually assume $\mu = \rho\nu$, with constant kinematic viscosity (e.g.,

Cook & Dimotakis 2001, Livescu & Ristorcelli 2007). In general, however, for mixing between incompressible fluids with different molar masses, μ is a weaker function of density. No study has been performed with real fluid variations of μ and $\mathcal{D}$, unlike the LMNOB equations used in thermal convection.

The nondimensional equations describing the incompressible mixing between two fluids with different molar masses, i.e., Equations 17, 18, and 29 [hereafter, the incompressible non-Boussinesq mixing (INBM) equations], are remarkably similar to the LMNOB equations. If one assumes $D \sim \mu/\rho$, with constant μ, then the INBM equations become the same as the LMNOB equations with constant material properties. However, since the T and ρ variations of the material properties are generally different, the distinction is maintained throughout this review. The INBM equations have been used in periodic domains (Section 3.4) (Sandoval 1995; Livescu & Ristorcelli 2007, 2008; Chung & Pullin 2010; D. Aslangil, D. Livescu & A. Banerjee, manuscript in review), VD RTI (Section 4.2) (e.g., Cook & Dimotakis 2001; Cabot & Cook 2006; Livescu et al. 2009, 2010, 2011), and several more complex flows, e.g., coupled RTI/Kelvin–Helmholtz instability (Olson et al. 2011) and inclined RTI (Andrews et al. 2014). Both sets of equations have been used for temporal shear-driven calculations (Section 4.1) (Almagro et al. 2017; Baltzer & Livescu 2019; J.R. Baltzer & D. Livescu, manuscript in review).

3.3. Boussinesq Limit

For a buoyancy-driven flow, where density variations arise due to thermal fluctuations, the OB approximation describes the thermomechanical response of linearly viscous fluids that can only undergo isochoric motions in isothermal processes. Rajagopal et al. (1996) derived these equations as a consistent third-order expansion using a small parameter that can be written as $\sqrt{Gr}/Re^{2/3}$ using the notations from Section 3.1.1. Starting from the single-fluid low-M equations, the OB approximation requires that the density variations appear in the momentum equations only in the buoyancy term, that material properties be constant, that dissipation be neglected in the temperature equation, that the continuity and temperature equations become identical scalar advection–diffusion equations, and that the divergence of velocity be zero,

$$\frac{\partial}{\partial t}\rho + \mathbf{u}\cdot\nabla\rho = \frac{1}{Pe}\nabla^2\rho, \tag{30.}$$

$$\frac{\partial}{\partial t}\mathbf{u} + \mathbf{u}\cdot\nabla\mathbf{u} = -\nabla\pi + \frac{1}{Re}\nabla^2\mathbf{u} + \frac{1}{Fr^2}\rho\mathbf{g}, \tag{31.}$$

$$\nabla\cdot\mathbf{u} = 0, \tag{32.}$$

where the Péclet number is $Pe = RePr$. The Boussinesq limit of the INBM equations is the same, with Pe replaced by the mass transfer Péclet number $Pe_{\mathrm{m}} = ReSc$.

To arrive at Equations 30–32 from the LMNOB or INBM equations, one requires that the density variations be small enough (Livescu & Ristorcelli 2007). From the momentum equation written in advection form, after division by density, this condition reads $1/\rho = 1/\rho_\infty(1 - \rho'/\rho_\infty + \cdots) \approx 1/\rho_\infty$, which is a zero-order approximation in $\rho' = \rho - \rho_\infty$. The condition also ensures that the material properties are constant. From the physical point of view, the largest temperature variations that can be used with the OB approximation can be quite different for various fluids. For example, at standard conditions, the maximum temperature difference for which the OB approximation is applicable is 28.6 K for air, but only 1.25 K for water (Gray & Giorgini 1976).

In the density equation, the Boussinesq diffusion term dominates for

$$|\nabla\rho|^2 \ll \frac{\rho}{2}|\nabla^2\rho|, \tag{33.}$$

$$|\nabla\rho|^2 \ll \rho|\nabla^2\rho|, \tag{34.}$$

for the LMNOB and INBM equations, respectively. Both conditions can be violated if substantial gradients develop in the density field, even at very low A. This subject is further explored in Section 3.5.

By comparing Equations 26 and 29 with Equation 31, one can see that $\nabla \cdot \mathbf{u}$ remains nonzero, even if Equation 31 is assumed valid. Therefore, to obtain Equations 31 and 32, one needs to further assume that Pe (or Pe_{m}) is large enough, so that the contributions from the dilatational (nonzero divergence) velocity component to the convective term and the viscous stress tensor are negligible in comparison to those of the solenoidal (zero divergence) part. The high–wave number range, however, presents an additional complication, since the dilatational kinetic energy, as it is set by density gradients, can become comparable to the solenoidal part (Livescu & Ristorcelli 2007).

An intermediate approximation to the LMNOB equations assumes that the background stratification remains fixed and the density variations are small compared to the background density gradient (Majda & Sethian 1985, Almgren et al. 2006a). While density variations may still be large enough to generate NOB effects, this anelastic approximation is not explored here. Instead, the reader is referred to the recent paper by Patel et al. (2016) and references therein for a discussion of some of these effects when property variations are nonnegligible but density fluctuations themselves are small.

3.4. Variable-Density Turbulence in a Triply Periodic Domain

The role of VD effects on the turbulence structure and mixing can be studied in greatest detail with numerical simulations in triply periodic domains, as one can achieve high accuracy calculations with large Reynolds number. Introduced by Batchelor et al. (1992) to investigate homogeneous buoyancy-driven turbulence (HBDT) under the Boussinesq approximation, this approach was extended to non-Boussinesq (NB) density variations by Sandoval (1995), Livescu & Ristorcelli (2007, 2008), and D. Aslangil, D. Livescu & A. Banerjee (manuscript in review) while retaining the homogeneity of the turbulent fields. Chung & Pullin (2010) proposed a triply periodic, inhomogeneous, but statistically stationary configuration of buoyancy-driven turbulence (SBDT) for a closer analogy with RTI. Inhomogeneous buoyancy-driven turbulence (IBDT) is another buoyancy-driven flow in a periodic domain that considers parallel vertical streams of different density fluids, with the mixing layer growing horizontally (Gat et al. 2017). The NB HBDT and SBDT studies have used the INBM equations with constant mass diffusivity and $\mu = \rho\nu$, while the IBDT study has used $\mathcal{D} = \mu/\rho$, for constant μ, which makes the equations equivalent to the LMNOB equations with constant properties. In all cases, Sc equals 1. As discussed in Section 4.1, these differences are likely to lead to only subtle changes for the lower-order statistics and are unlikely to qualitatively affect the results, at least for the range of parameters studied.

With periodic boundary conditions, the Poisson equation for pressure can be solved up to a constant gradient. By requiring that the time derivative of the mean velocity be nonnegative in the direction of gravity (which ensures an unstable configuration), one can maximize the growth rate of the vertical mass flux $\langle\rho\mathbf{u}'\cdot\mathbf{g}\rangle/\langle\rho\rangle$ by choosing $\langle\mathbf{u}\rangle = 0$, $\nabla\langle p\rangle = \frac{1}{V}\left(\frac{1}{Fr^2}\mathbf{g} - \langle v\nabla p'\rangle + \langle\mathbf{u}'\Delta\rangle + \langle v\nabla\cdot\boldsymbol{\tau}\rangle\right)$, where primes denote fluctuations, i.e., $\mathbf{u}' = \mathbf{u} - \langle\mathbf{u}\rangle$, and

$v = (\frac{1}{\rho})'$ and $V = \langle \frac{1}{\rho} \rangle$ are the fluctuating and mean specific volume, respectively (Livescu & Ristorcelli 2007). These conditions are also approximately satisfied in the central region of the RTI turbulent mixing layer (Livescu et al. 2009). Chung & Pullin (2010) used similar conditions at the centerline plane, coupled with a nonzero mean density gradient and fringe layers at the top and bottom boundaries, in order to sustain the stationarity of the flow. On the other hand, Gat et al. (2017) chose $\nabla\langle p \rangle$ such that the mean vertical mass flux is constant, which ensures that the mixing layer grows horizontally.

In HBDT, the two different-density fluids are initially segregated into large patches and start to move in opposite directions due to the acceleration field, generating turbulence motions, which in turn enhances mixing. Initially, the ratio of production ($\mathcal{P}$) to dissipation (ϵ) of TKE is large ($\mathcal{P}/\epsilon \gg 1$) and decays with time as the fluids mix. As a result, TKE first has a growth stage, reaches a maximum for $\mathcal{P}/\epsilon = 1$, and then decays. The flow may show some similarities with RTI during the growth stage and with late-time RMI during the decay stage. As shown by Batchelor et al. (1992), due to the presence of buoyancy, the nonlinear effects cannot be neglected during the decay stage, even at $t \to \infty$ as A tends to zero. The buoyancy-mediated turbulence decay is very different from classical turbulence decay. Depending on the infrared shape of the density spectrum, Re_λ can grow indefinitely or approach a constant, as TKE continues to decay while the turbulence length scale increases faster (Batchelor et al. 1992; D. Aslangil, D. Livescu & A. Banerjee, manuscript in review).

However, IBDT is a constant acceleration version of the classical shear-driven mixing layer problem (which has constant mean velocity), as discussed in Section 4.1, and has similarities with vertical convection in infinitely long domains, as discussed in Section 4.3. Since the mean density and pressure gradients are perpendicular, the configuration also maximizes the baroclinic production of vorticity. Thus, the mixing layer width, h, reaches a fast self-similar growth stage with $h \sim t^3$.

As explained in the subsequent sections, all three points (see the sidebar titled Key Features of VD Turbulent Flows) are consequences of differential fluid inertia; the first two points can be associated with stirring and mixing, respectively, as defined by Villermaux (2019), while various asymmetries of the mixing layers might result from a combination of differential entrainment, stirring, and mixing. In addition, for $\mathcal{P}/\epsilon \gg 1$ (e.g., in HBDT, SBDT, and RTI), as η_K becomes smaller, the dissipation scales remain anisotropic even as the flow develops an inertial range (Livescu & Ristorcelli 2008, Livescu et al. 2009, Chung & Pullin 2010). In such strongly nonequilibrium conditions, buoyancy production is still felt at the smallest scales, due to a leading-order cancelation between nonlinear and viscous effects in the dissipation range.

These characteristics also appear in shock–isotropic VD turbulence interaction and RMI and will be explored in more detail in the flow examples surveyed below. In particular, the asymmetric behavior of the density PDF can be inferred from the density skewness ($S = \langle \rho'^3 \rangle / \langle \rho'^2 \rangle^{3/2}$)

KEY FEATURES OF VD TURBULENT FLOWS

As A becomes large, all VD canonical turbulent flows display several features. (*a*) Turbulence characteristics are different in the light- and heavy-fluid regions, with more intense turbulence within the light-fluid regions. (*b*) Density and mole fraction PDFs become asymmetric, with the peak below the average value, and the pure light-fluid regions mix faster than the pure heavy-fluid regions. (*c*) When present, mixing layers become asymmetric, with a larger width on the light-fluid side and various neutral points moving off of the original centerline; the light-fluid side is always rougher than the heavy-fluid side.

equation, which can be derived from the continuity equation and divergence of velocity (Equation 29). For the homogeneous configuration, this is (Livescu & Ristorcelli 2009, Livescu et al. 2010)

$$\frac{\partial}{\partial t}S = 3\frac{\langle \nabla\rho' \cdot \nabla\rho' \rangle}{Pe_{\mathrm{m}}\langle \rho'^2 \rangle}\left(S - 2\frac{\langle \rho' \nabla\rho' \cdot \nabla\rho' \rangle}{\langle \rho'^2 \rangle^{1/2}}\right). \tag{35.}$$

The quantity $\langle \rho' \nabla\rho' \cdot \nabla\rho' \rangle$ is weighted toward large squared–density gradient events occurring in lower-than-average density regions so that S increases, even when S equals zero initially. This can be seen from the transport equation for the density gradient squared (Livescu et al. 2010), where the production term is proportional to $-\langle \nabla\rho \cdot \mathbf{s} \cdot \nabla\rho \rangle$, where $\mathbf{s}$ is the strain rate tensor. Thus, in the light-fluid regions, the density gradients are better aligned with the eigenvectors of $\mathbf{s}$, as the lower inertia allows the fluid to respond faster to changes in the local strain. In other words, the light-fluid regions become more fragmented at higher A, molecular mixing is faster, and density skewness becomes positive. For the LMNOB equations in a homogeneous configuration, the skewness equation can be written as

$$\frac{\partial}{\partial t}S = 3\frac{\langle (\nabla\rho' \cdot \nabla\rho')/\rho \rangle}{Pe\langle \rho'^2 \rangle}\left[S - 2\frac{\langle \rho' (\nabla\rho' \cdot \nabla\rho')/\rho \rangle}{\langle \rho'^2 \rangle^{1/2}}\right], \tag{36.}$$

showing a similar mechanism for positive skewness generation, although the details of the molecular mixing may be different.

3.5. Regularity Considerations

As explained in Section 3.3, even when A is very small, it is not clear a priori that the density gradients should remain small, or the flow may develop regions where conditions of Equations 33 and 34 are violated (Rao et al. 2017). By defining an effective velocity equal to the solenoidal velocity component,

$$\mathbf{v} = \mathbf{u} + Pe_{\mathrm{m}}^{-1}\nabla(\ln\rho), \quad \text{with} \quad \nabla\cdot\mathbf{v} = 0 \quad \text{and} \quad \nabla\times\mathbf{v} = \nabla\times\mathbf{u}, \tag{37.}$$

the INBM continuity equation becomes an advection–diffusion equation,

$$\frac{\partial}{\partial t}\rho + \mathbf{v}\cdot\nabla\rho = \frac{1}{Pe_{\mathrm{m}}}\nabla^2\rho, \tag{38.}$$

formally the same as the Boussinesq approximation. However, the fact that $\mathbf{v}$ is actually an (explicit) function of ρ makes Equation 38 less simple than it first appears. Nevertheless, this equation can be used to make some qualitative assessments of the mixing dynamics. Following Rao et al. (2017), consider a 1D horizontal section through a rightward-moving density wave at a snapshot in time. In the frame of the advecting velocity $\mathbf{u}$, the relevant component of $\mathbf{v}$ is greater on the back face of the wave at any position (since $\nabla\rho > 0$) than on the front face (where $\nabla\rho < 0$). Thus, in the advecting frame, Equation 38 implies that there is a natural tendency for the back of a wave to catch up with the front, thus leading to a natural and inevitable steepening of $\nabla\rho$.

A similar transformation for the LMNOB equations, $\mathbf{v} = \mathbf{u} - Pe^{-1}\nabla(\frac{1}{\rho})$, with $\nabla\cdot\mathbf{v} = 0$ and $\nabla\times\mathbf{v} = \nabla\times\mathbf{u}$, leads to a more complicated continuity equation,

$$\frac{\partial}{\partial t}\rho + \mathbf{v}\cdot\nabla\rho = \frac{1}{Pe}\frac{1}{\rho}\nabla^2\rho, \tag{39.}$$

as the diffusion term remains nonlinear. Nevertheless, the same type of heuristics might be invoked to show the tendency toward steepening of the density waves. However, due to the differences in the magnitudes of $\nabla(\ln\rho)$ and $\nabla(1/\rho)$, one might expect different diffusion layer shapes.

While the density itself is bounded, Equations 38 and 39 show the importance of density gradients to the rate of irreversible mixing within the flow. By taking advantage of the transformation $\theta = \ln \rho$, which makes the INBM continuity equation linear in θ,

$$\frac{\partial}{\partial t}\theta + \mathbf{u} \cdot \nabla\theta = \frac{1}{Pe_{\mathrm{m}}}\nabla^2\theta, \qquad 40.$$

Rao et al. (2017) were able to write transport equations for higher-order moments of $\nabla\theta$,

$$\Omega_{m,\theta} = \left(\int_{\mathcal{V}} |\nabla\theta|^{2m} \mathrm{d}V\right)^{1/2m}. \qquad 41.$$

Following the procedure proposed by Donzis et al. (2013), Gibbon et al. (2014), and Gibbon (2015) for higher-order moments of vorticity, $\Omega_{m,\omega} = \left(\int_{\mathcal{V}} |\boldsymbol{\omega}|^{2m} \mathrm{d}V\right)^{1/2m}$, with $\boldsymbol{\omega} = \nabla \times \mathbf{u}$, in isotropic turbulence, Rao et al. (2017) also found analytical bounds for the terms in the $\Omega_{m,\theta}$ transport equation. Then, they evaluated these bounds using the low-A DNS data set of triply periodic HBDT satisfying the INBM equations from the Johns Hopkins Turbulence databases (Livescu et al. 2014). The results showed that nonlinear depletion is appreciably weaker in the density gradient field compared to vorticity field. The fast growth of the density gradients leaves open the possibility of blowup in finite time for large-enough Pe_{m} or small-enough Fr values, even when A is nominally near the Boussinesq limit. Aslangil et al. (2017) and D. Aslangil, D. Livescu & A. Banerjee (manuscript in review) extended the analysis to higher A and found that density gradients are much larger in light-fluid regions compared to heavy-fluid regions, which also have higher levels of turbulence fluctuations and mix faster. Thus, if a blowup occurs, it is in the light-fluid regions. Of course, the loss of regularity would invalidate the incompressible assumption and restrict the mathematical model to a certain region of the parameter space (Re, Sc, and Fr). Such a result would be quite remarkable in the presence of viscous and diffusive effects. In the spirit of Beale et al. (1984), one can write the transport equation for the curl of momentum per unit volume, $\boldsymbol{\omega}^* = \nabla \times (\rho\mathbf{u})$, so that the baroclinic term does not appear in the equation. For the inviscid case, the equation shows that the maximum norm of $\boldsymbol{\omega}^*$ is also controlled by the density gradients, in addition to vortex stretching, displaying multiple paths for the breakdown of regularity.

3.6. Locality of the Turbulence Cascade in Variable-Density Turbulence

The development of an inertial range of scales and the subsequent mixing transition rely on the viscous effects being restricted to a viscous range (Eyink 2005). However, for VD turbulence, such scale decomposition is not as straightforward as in incompressible flows. In particular, it is possible that certain quantities exhibit viscous effects at all scales, while others do not (Aluie 2013, Zhao & Aluie 2018). Using a coarse-grained filtering defined by $\bar{\mathbf{a}}_l(\mathbf{x}) = \int \mathrm{d}^n\mathbf{r} G_l(\mathbf{r})\,\mathbf{a}(\mathbf{x}+\mathbf{r})$, where $G(\mathbf{r})$ is a normalized convolution kernel and $G_l(\mathbf{r}) = l^{-n}G_l(\mathbf{r}/l)$ is a dilated version of the kernel having its main support over a region of diameter l, Aluie (2013) and Zhao & Aluie (2018) analyzed the viscous contributions to scale l for three versions of the large-scale TKE (TKE_l): $\mathrm{TKE}_l^{\mathrm{F}} = \overline{\rho}_l|\tilde{\mathbf{u}}_l|^2/2$, $\mathrm{TKE}_l^{\mathrm{C}} = \overline{\rho}_l|\overline{\mathbf{u}}_l|^2/2$, and $\mathrm{TKE}_l^{\mathrm{K}} = |\overline{(\sqrt{\rho}\mathbf{u})}_l|^2/2$. The Favre-filtered velocity is defined by $\tilde{\mathbf{u}}_l = \overline{(\rho\mathbf{u})}_l/\overline{\rho}_l$. The Favre filtering has been used extensively in large eddy simulations (LES) of compressible and VD turbulence (e.g., Garnier et al. 2009), $\mathrm{TKE}_l^{\mathrm{C}}$ is written by analogy with the incompressible case, and $\mathrm{TKE}_l^{\mathrm{K}}$ is constructed to yield a quadratic form.

As **Figure 4** shows, only the Favre formulation has a vanishing viscous contribution at large scales, as k tends to zero. This is consistent with current LES approaches. However, the proof given by Zhao & Aluie (2018) also suggests that some of the terms in current RANS (Reynolds-averaged

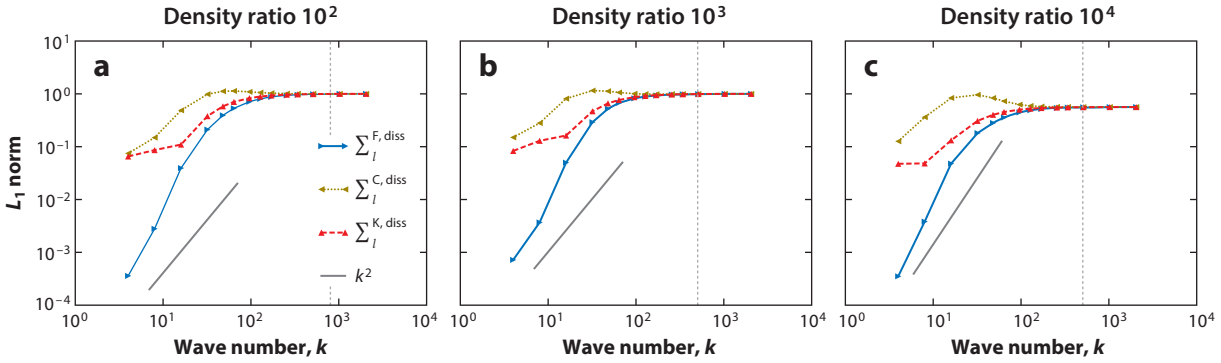

Figure 4

L_1 norm of the viscous contributions, $\Sigma_l^{i,\mathrm{diss}}$, normalized by the maximum dissipation, to the turbulent kinetic energy (TKE) equation filtered at scale l, using three different TKE definitions, as a function of the wave number $k = L_z/l$, where L_z is the vertical domain size. The vertical line in each figure marks the viscous cut-off wave number, $k_\mathrm{d} = L_z/\eta_\mathrm{K}$, where η_K is the Kolmogorov microscale. The upper index i corresponds to TKE defined by $\mathrm{TKE}_l^\mathrm{F} = \overline{\rho}_l|\tilde{\mathbf{u}}_l|^2/2$, $\mathrm{TKE}_l^\mathrm{C} = \overline{\rho}_l|\overline{\mathbf{u}}_l|^2/2$; and $\mathrm{TKE}_l^\mathrm{K} = |\left(\sqrt{\rho}\mathbf{u}\right)_l|^2/2$. For comparison, the k^2 variation is also shown. Data correspond to Rayleigh–Taylor instability turbulence at density ratios (*a*) 10^2, (*b*) 10^3, and (*c*) 10^4. Figure adapted with permission from Zhao & Aluie (2018).

Navier–Stokes) modeling of Favre TKE, e.g., $\langle\rho|\mathbf{u}''|^2\rangle/2$, may retain viscous contributions at all scales, irrespective of the Reynolds number, if the density variations are large enough. Here, $\mathbf{u}''$ are the Favre velocity fluctuations. Corresponding spectral formulations may also have a similar problem. This is an intriguing possibility that needs further study. A quadratic form of TKE that is consistent with the inviscid scale decomposition is based on the fluctuating momentum, $\mathrm{TKE}''' = |\rho\mathbf{u}''|^2/\langle\rho\rangle$. Indeed, TKE''' spectra show a reduced viscous range compared to the usual quadratic formulations (i.e., TKE^C and TKE^K) in HBDT (D. Aslangil, D. Livescu & A. Banerjee, manuscript in review) and RMI turbulence (Wong et al. 2019).

4. LOW–MACH NUMBER AND INCOMPRESSIBLE VARIABLE-DENSITY FLOW EXAMPLES

Here, numerical and experimental results concerning turbulence characteristics in several canonical flows are discussed. While the literature on each of the flows is vast, the discussion is restricted to large thermal and compositional density effects (so that $A \gtrsim 0.1$) and the reader is referred to the appropriate reviews for other flow physics. Additional canonical VD turbulent flows include jets and wakes (Amielh et al. 1996, Chassaing et al. 2002, Gerashchenko & Prestridge 2015, Charonko & Prestridge 2017) and shock–bubble interactions (Ranjan et al. 2011).

4.1. Temporal Variable-Density Shear-Driven Mixing Layers

Turbulence sustained by shear between streams of fluids is a fundamental phenomenon relevant to a wide range of applications in combustion, industrial engineering, geophysical flows, and so on (Givi 1989, Dimotakis 2005, O'Brien et al. 2014). Shear-driven mixing layers have historically received a great deal of attention, but mainly for high-speed or reacting configurations, where compressibility and heat release play a central role (Vreman et al. 1996, Freund et al. 2000, Miller et al. 2001, Pantano & Sarkar 2002). Brown & Roshko (1974) experimentally studied a low-speed spatially developing VD mixing layer and found reductions in the growth rates as large as 50% for density ratios up to 7. The measurements were limited to mean density and streamwise velocity

profiles and did not investigate the associated turbulence or mixing changes. Brown (1974) proposed a formula for the growth rate variation with A based on the assumption that the temporal growth rate (i.e., in a frame of reference moving with the mixing layer convection velocity, which is closer to the high-density stream velocity) is independent of the density difference between streams. Dimotakis (1984) refined the formula to account for asymmetric entrainment, and Gat et al. (2017) further discussed the convective velocity in the context of their IBDT flow.

Most numerical simulations address the temporal case, due to the convenience of using periodic boundary conditions in two directions and higher achievable Reynolds numbers, although the spatially developing case, with direct experimental comparisons, has also been considered (Attili & Bisetti 2012). The pioneering temporal simulations of Pantano & Sarkar (2002) included an investigation of different freestream densities, albeit at moderately high speed (convective Mach number of $M_c = 0.7$) within a broader study of compressible mixing layers. The simulations were performed for a single fluid with thermal density variations. Overall, they found that increasing the density difference between the streams substantially decreases the temporal thickness growth rate defined in terms of momentum thickness, but the growth rate of the vorticity thickness experiences a weaker reduction. The simulations revealed that the Reynolds shear stress changes little in magnitude with increasing A but shifts to the light-fluid side. They also developed a model characterizing the shift of the mean velocity profile to the light-fluid side and the associated decrease in the momentum thickness growth rate. Ashurst & Kerstein (2005) used the 1D turbulence stochastic simulation method to explore the VD effects in temporal and spatial mixing layers. They successfully captured many of the effects observed by Pantano & Sarkar (2002). More recently, Almagro et al. (2017) addressed the low-speed case of Pantano & Sarkar (2002) using the constant-coefficient LMNOB equations, while J.R. Baltzer & D. Livescu (manuscript in review) performed large-resolution DNS of temporal VD mixing layers using the INBM equations with A up to 0.87, corresponding to a hydrogen–air system.

For the three VD configurations addressed by Pantano & Sarkar (2002), Almagro et al. (2017), and J.R. Baltzer & D. Livescu (manuscript in review), the self-similar analysis remains the same. Thus, the self-similar forms of the continuity and momentum equations are (Pantano & Sarkar 2002)

$$(\hat{U}_2 - \eta)\hat{\rho}' + \hat{\rho}\hat{U}_2' = 0, \qquad 42.$$

$$(\hat{U}_2 - \eta)\hat{\rho}\hat{U}_1' + (\hat{\rho}\hat{R}_{12})' = 0, \qquad 43.$$

where the mean variables have been normalized using scalings suggested by the self-similar analysis:

$$\hat{\rho}(\eta) = \frac{\langle\rho\rangle(y,t)}{\rho_0}, \quad \hat{U}_1(\eta) = \frac{\tilde{U}_1(y,t)}{\Delta U}, \quad \hat{U}_2(\eta) = \frac{\tilde{U}_1(y,t)}{\mathrm{d}h/\mathrm{d}t}, \quad \hat{R}_{12}(\eta) = \frac{\tilde{R}_{12}(y,t)}{\Delta U\,\mathrm{d}h/\mathrm{d}t}, \qquad 44.$$

where ρ_0 is the initial centerline density, ΔU is the difference between the freestream velocities, the self-similarity variable is defined by $\eta = y/h$, the primes denote derivatives with respect to η, the tilde denotes Favre averaging (i.e., $\tilde{U}_1 = \langle\rho U_1\rangle/\langle\rho\rangle$), and $\tilde{R}_{12}$ is the Favre-averaged Reynolds shear stress. The coordinate system is chosen with 1, 2, and 3 as the streamwise, cross-stream (inhomogeneous), and spanwise (homogeneous) directions. The self-similar growth rate $\mathrm{d}h/\mathrm{d}t$ is constant, but decreases with A. Analytical and numerical analyses of the self-similar equations (Pantano & Sarkar 2002; J.R. Baltzer & D. Livescu, manuscript in review) have revealed that the layer becomes asymmetric and that the peaks and zero-crossing points of various profiles move to the light-fluid side. Thus, **Figure 5*a*** shows the locations

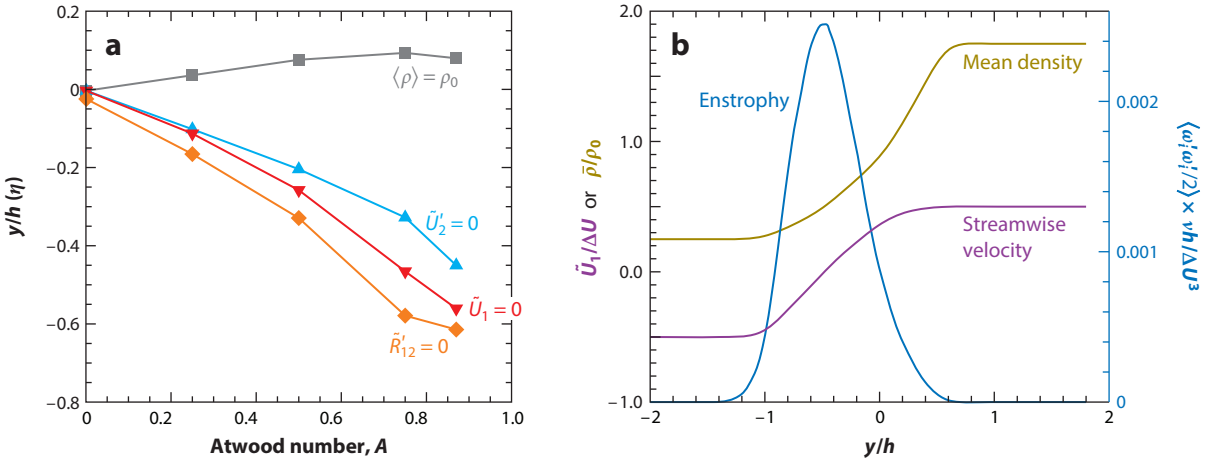

Figure 5

(*a*) Drifts of the locations where we have $\langle\rho\rangle = \rho_0$ (*gray*), $\tilde{U}_2' = 0$ (*blue*), $\tilde{U}_1 = 0$ (*red*), and $\tilde{R}_{12}' = 0$ (*orange*) as a function of A. (*b*) Profiles of mean density, streamwise velocity, and enstrophy at $A = 0.75$. Abbreviations: A, Atwood number; η, self-similarity variable; h, mixing layer width; $\tilde{R}_{12}'$, derivative of the Favre-averaged Reynolds stress; $\langle\rho\rangle$, average density; ρ_0, initial centerline density; ΔU, magnitude of the difference between freestream velocities; $\tilde{U}_1$, Favre-averaged streamwise velocity; $\tilde{U}_2'$, derivative of the Favre-averaged spanwise velocity. Figure adapted from J.R. Baltzer & D. Livescu (manuscript in review).

of the points $\tilde{U}_1 = 0$, $\tilde{U}_2' = 0$, and $\tilde{R}_{12}' = 0$, denoted hereafter by η_1, η_2, and η_{12}, respectively, as a function of A. For large-A values, these locations drift significantly away from the centerline, with $\eta_{12} < \eta_1 < \eta_2 < 0$, as the larger inertia of the heavy fluid breaks the entrainment symmetry in the central regions of the layer. While the neutral density point (i.e., the location $\langle\rho\rangle = \rho_0$) does not move much from the centerline at higher A, the mean density profile also becomes asymmetric. As indicated by **Figure 5*b***, the profile becomes steeper on the heavy-fluid side and shallower on the light-fluid side. In addition, the density PDF becomes skewed, with more pure heavy fluid reaching the centerline compared to pure light fluid (Baltzer & Livescu 2019). This is also consistent with experimental data (Koochesfahani & Dimotakis 1986). Furthermore, turbulence itself becomes more intense on the light-fluid side. For example, most enstrophy is located below the centerline (**Figure 5*b***). As a result, the density field is significantly rougher (more fragmented) on the light-fluid side (**Figure 6**). All these features are qualitatively similar among the three shear-driven configurations compared here and are consistent with all other VD flows discussed in this review.

4.1.1. Contrasting thermal and compositional density variations. While temporal mixing layer results show many qualitatively similar features among the fully compressible layer with thermal density variations, the LMNOB case (with constant molecular coefficients), and the INBM case (with $\mu = \rho\nu$), Baltzer & Livescu (2019) have made a direct comparison between the latter two cases. As expected, the mean density and velocity profiles match closely during the self-similar growth, with some differences in the shifts discussed above (**Table 1**). With the same dynamic viscosity variation, the vertical velocity peak moves to lighter-fluid regions in the LMNOB case. However, when the dynamic viscosity is constant (as in the simulations of Almagro et al. 2017), the LMNOB profile shifts become closer to the variable-viscosity INBM shifts. All higher-order statistics display similar qualitative features, but some quantitative differences. For example, density PDFs present a more pronounced asymmetry for the LMNOB configurations. It is not known how these differences change with Re or Re_m values.

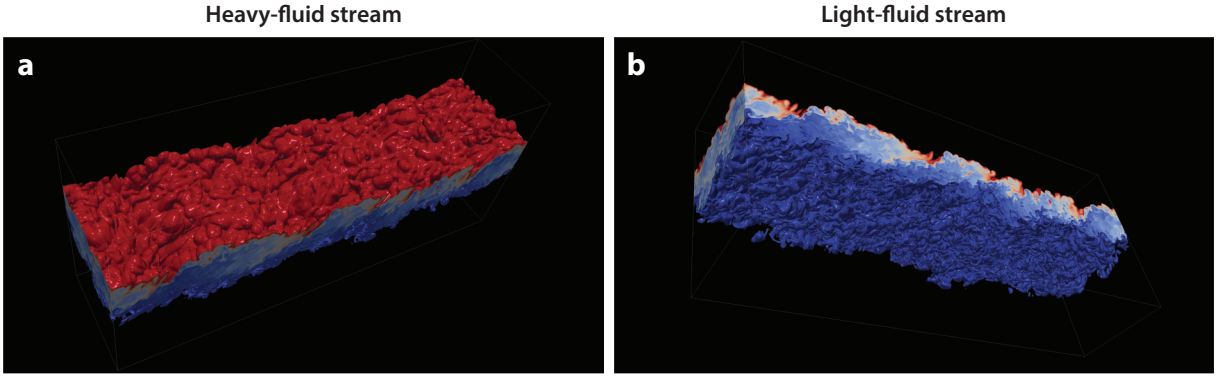

Figure 6

Density isosurfaces near the heavy-fluid (*a*) and light-fluid (*b*) streams from a temporal mixing layer direct numerical simulation with Atwood number $A = 0.75$. Figure adapted from J.R. Baltzer & D. Livescu (manuscript in review).

4.2. Rayleigh–Taylor Instability with Miscible Incompressible Fluids

Classical RTI (Chandrasekhar 1981, Sharp 1984, Youngs 1984) arises at the interface between two different density fluids in the presence of a constant acceleration pointing opposite to the density gradient. Small perturbations of the initial interface grow, interact nonlinearly, and lead to turbulence. Compared to its classical formulation, in most practical cases, RTI manifests itself as an extremely complex process. The complexity arises due to an intertwined manifold of factors, among which are the density difference, compressibility, temperature distribution, viscosity, surface tension and other interfacial phenomena (for the immiscible case), mass diffusion (for the miscible case), heat diffusion, geometrical and finite boundary effects, specific plasma and magnetic field properties, and so on. As such, flows featuring RTI-type growth of instabilities can be found in several important natural phenomena and applications, for example, in supernova explosions and neutron stars; the solar corona; Earth's oceans, atmosphere, and mantle; quantum plasma; combustion; ICF; sonoluminescence; industrial coating with thin liquid films, etc. [e.g., see Cabot & Cook (2006); Livescu (2013); Swisher et al. (2015); Boffetta & Mazzino (2017); Zhou (2017a,b); Remington et al. (2019); and references therein].

For single-fluid flows with significant thermal density differences, the temperature is finite and the hydrostatic balance in the momentum equations results in large pressure variations. Therefore, as the instability develops, the background pressure cannot be assumed uniform or constant in time and the use of the LMNOB equations is not justified for large A. Thus, for this configuration, NB effects require fully compressible treatments. Results concerning the Boussinesq limit were summarized by Boffetta & Mazzino (2017). The role of strong background stratification has been discussed by Gauthier (2017). Nevertheless, NB effects can be isolated from compressibility effects

Table 1 y/b **values for INBM and LMNOB shear-driven turbulence with Atwood number of 0.75**

Equations type	η_ρ ($\langle\rho\rangle = \rho_0$)	η_2 ($\tilde{U}_2$ peak)	η_1 ($\tilde{U}_1 = 0$)	η_{12} ($\tilde{R}_{12}$ peak)
INBM with $\mu = \rho\nu$	0.07	−0.36	−0.43	−0.55
INBM with constant μ	0.07	−0.27	−0.44	−0.54
LMNOB with $\mu = \rho\nu$	0.08	−0.31	−0.44	−0.54
LMNOB with constant μ	0.07	−0.37	−0.45	−0.53

Here b is defined based on 10% and 90% of the mean velocity profile. Table adapted with permission from Baltzer & Livescu (2019).

using the INBM equations, for a configuration where the density variations arise from fluids with different molar masses.

RTI with quasi-incompressible miscible fluids and NB effects has been addressed both experimentally, by Banerjee et al. (2010) for A up to 0.6 and Akula & Ranjan (2016) for A up to 0.73, and numerically by Cook & Dimotakis (2001), Cabot & Cook (2006), and Livescu et al. (2009, 2010) for $A = 0.5$; by Livescu et al. (2011) and Livescu (2013) for A up to 0.9; and by Cabot & Zhou (2013) for A up to 0.8. Larger A values have been addressed in experiments using immiscible fluids [e.g., A up to 0.96 (Dimonte & Schneider 2000)] and under-resolved simulations with numerical stabilization (e.g., Dimonte et al. 2004, Youngs 2013, and references therein). However, the differences between immiscible and miscible cases, as well as numerical versus physical diffusion effects on RTI turbulence, are still open questions.

The self-similar solution to the RTI problem is represented by a quadratic law for the mixing layer growth (Ristorcelli & Clark 2004),

$$h = \alpha g t^2 + 2\left(\alpha A g h_0\right)^{1/2} + h_0. \qquad 45.$$

The value of the growth rate coefficient α has been central for much of the RTI research (Dimonte et al. 2004, Youngs 2013) and is still subject to active debate (Youngs 2017). There is also some inconsistency in the literature about including the linear term in the growth formula, which can lead to large differences at early times (Cabot & Cook 2006). The connection between α and the very-low-frequency components of the initial perturbation (e.g., Ramaprabhu et al. 2005, Livescu et al. 2011, Youngs 2013, Roberts & Jacobs 2016) makes the problem challenging to address both experimentally, where the control of the initial perturbation is notoriously difficult, and numerically, since it would require extremely large resolutions—recent advances in experimental setups (Roberts & Jacobs 2016) and computational power notwithstanding. Current results seem to indicate that, if the initial perturbation spectrum contains only high–wave number components, relatively low values for the growth coefficient obtain, i.e., $\alpha \sim 0.025$–0.03 (Livescu et al. 2010, Youngs 2013). However, with a spectrum of the type $E(K) \sim k^{-3}$, which is significantly weighted toward the low–wave number region, much larger values are obtained, $\alpha \sim 0.06$–0.1 (Livescu et al. 2011, Youngs 2013), typical to the experimental range (Banerjee & Andrews 2006). Similarly, the mixedness Θ asymptotes to around 0.8 when only high–wave number components are present in the initial perturbation, while the initial perturbation spectrum of k^{-3} leads to lower values of around 0.7 (Youngs 2013). The mixing layer becomes strongly asymmetric as A increases, with $h_s/h_b \sim [(1+A)/(1-A)]^n$, where values of n in the range 0.23–0.33 have been reported (Dimonte & Schneider 2000, Youngs 2013). This asymmetry is largely due to the increase in the growth rate on the spike side. More details about these values can be found in the recent review by Zhou (2017a,b).

In principle, the single-mode perturbation may be relevant to this problem, although a diverse class of models assumes a qualitatively different growth formula than Equation 45, with constant asymptotic velocity. There is indication, however, that the layer reaccelerates at later times (Ramaprabhu et al. 2006) and may, in fact, grow quadratically at sufficiently high Reynolds number (Wei & Livescu 2012). In this case, single-mode RTI may represent an upper bound for the multimode case, consistent with the faster growth seen for the initial perturbation spectrum concentrated at small wave numbers. Nevertheless, even the largest α values reported experimentally at moderate A are still much smaller than the free-fall value of 0.5, indicating significant energy transfer to the horizontal motions, as required for the development of turbulence. Indeed, the normal Reynolds stress anisotropy seems to vary little with A and across the layer, with $b_{33} \approx 0.3$ (so that the vertical component has about the same kinetic energy as the sum of the horizontal

components) (Livescu et al. 2010). In principle, the theoretical limit as A approaches unity is $\alpha = 0.5$ (see above references and the recent reviews by Zhou 2017a,b). However, it is not clear if this limit is achievable or if the mathematical model (INBM equations or even the fully compressible equations) becomes inadequate at some $A < 1$, since the velocities quickly become large.

There is a proliferation of theoretical models for the spectral scaling and dynamics of low-A RTI turbulence owing to the variety of possible dynamical regimes (Boffetta & Mazzino 2017); however, it is not clear how these models can be extended to the NB case, especially if an inviscid scale decomposition criterion is required (see Section 3.6).

From the point of view of the VD effects, current simulations and experimental results with finite A values are consistent with those described throughout this review: (*a*) The RTI mixing layer becomes asymmetric, rougher and faster growing on the light-fluid side (showing so-called spikes), and smoother and slower growing on the heavy-fluid side (showing so-called bubbles) (this is qualitatively similar with RMI and shear-driven mixing layers); (*b*) turbulence intensities are larger in light-fluid regions than heavy-fluid regions; and (*c*) mixing is asymmetric, with pure heavy fluid reaching larger depths from the layer edge than pure light fluid.

4.3. Thermal Convection

Convection driven by temperature differences is ubiquitous in nature, e.g., geophysical flows, the interiors of stars, and industrial engineering. The study of thermal convection has been an active field of research for over a century. Several important model problems include: Rayleigh–Bénard (RB) convection (Lohse & Xia 2010), where a cavity is heated from below and cooled from above; horizontal convection (Hughes & Griffiths 2008), where the heating occurs at the same level, for example, on the bottom surface; and vertical convection or differentially heated cavities (DHC) (e.g., Paolucci & Chenoweth 1989, Fusegi et al. 1990, Wang et al. 2019), where the cavity is heated/cooled from the sides. The literature is rich with variations of these basic problems such as changes in the aspect ratios, open cavities, and the additions of rotation, plasma and magnetic effects, radiation, etc.

In the typical RB problem, due to the background stratification, NOB effects are usually considered in the anelastic approximation for the continuity equation, with additional approximations for the momentum equations within the boundary layers (e.g., Ahlers et al. 2007). While the resulting Atwood numbers are small (generally $A < 0.1$ for gases and $A \approx 0$ for liquids), the viscosity and heat conduction variations with temperature are large enough to produce a top-down statistical symmetry breaking in the temperature drops across the boundary layers and a drifting of the mean temperature off of the center. The effects of density and material properties variations can be qualitatively separated by comparing experimental results using liquids and gases (Ahlers et al. 2006, 2007). Thus, for liquids, where density is quasi-constant, the larger bottom boundary layer induces a larger center temperature. For gases, the associated decrease in density and volumetric expansion leads to a faster decrease in temperature away from the wall and, thus, a reduced center temperature.

Larger temperature differences (and A values) have been studied in vertical convection. The flow is characterized by two boundary layers near the heated and cooled vertical sides and by two intrusion layers near the horizontal walls, which complete a recirculation pattern. The net energy surplus transferred upward by both boundary layers is balanced by heat conduction through the main body of the cavity. Wang et al. (2019) performed 2D simulations with the LMNOB equations, nominally for air, up to $A = 0.6$. In this case, NOB effects break the left–right antisymmetry, with the thermal and viscous boundary layers thicker near the hot plate and thinner near the cold plate and a larger center temperature compared to the OB limit. These results are qualitatively

different than those obtained for RB convection, where the center temperature is reduced for gases in the presence of NOB effects. Thus, due to different inertia of the light- and heavy-fluid streams, the differential entrainment in DHC moves the neutral density point (i.e., where the density is equal to the average of the light- and heavy-fluid stream), as well as the neutral temperature point, to the heavy-fluid side. This is qualitatively similar to shear-driven turbulence (Section 4.1) and IBDT turbulence results discussed in Section 3.4. Recent results (e.g., Wang et al. 2019) have seemed to indicate that the overall integrated quantities (e.g., Nusselt number) are not affected by NOB effects after the onset of stationarity. It would be interesting to see if this result changes in 3D for fully turbulent flows. For example, as the *Ra* value for the transition to turbulence may depend on *A*, the Nusselt scaling may change as well. From the point of view of turbulence structure, it is likely that the VD effects highlighted earlier, with more intense turbulence in the light-fluid regions and different molecular mixing characteristics of the pure light-fluid and heavy-fluid regions, would be maintained for this flow as well. Again, it would be interesting to study if these local changes affect any of the global parameters of the flow.

SUMMARY POINTS

1. Density variations due to thermal and compositional fluctuations produce similar effects as the flow interacts with a shock wave or the shock propagates through a variable-density (VD) medium.
2. The equations describing the single-fluid low–Mach number approximation for flows with thermal variations and the incompressible limit of binary mixing of fluids with different molar masses are remarkably similar, with some differences in the transport terms.
3. Strong inertial effects associated with density variations lead to significant asymmetries in turbulence stirring and entrainment, affecting the growth of mixing and boundary layers, while subtle differences in the transport formulations change the dynamics of the density gradients and molecular mixing. The effects are shared by VD turbulence evolution away from a shock wave, Richtmyer–Meshkov instability (RMI), Rayleigh–Taylor instability, shear-driven mixing layers, and vertical convection.
4. Density variations may change the regularity properties of the underlying incompressible Navier–Stokes equations.
5. In the presence of strong VD effects, the kinetic energy spectrum needs to be formulated consistent with the inviscid-scale decomposition criterion to avoid viscous contamination at large scales.

FUTURE ISSUES

1. VD effects, as well as similarities and differences between thermal and compositional density variations, need to be explored at higher Péclet number (*Pe*) and mass diffusion Péclet number, Pe_m. In particular, what is the interplay between stirring and molecular mixing as *Pe* and Pe_m tend to infinity?
2. Experiments with miscible materials and large density ratios are needed to further explore the physics of VD turbulence as well as the validity of the LMNOB (low–Mach number, non-Oberbeck–Boussinesq) and INBM (incompressible non-Boussinesq mixing) approximations.

3. Experiments with tighter control of the initial conditions as well as measurements of higher-order turbulence statistics are desired to produce more accurate scaling laws for the light-fluid and heavy-fluid sides of mixing layers, and to better inform the models and explore VD effects for flows or regimes where DNS remains out of reach, for example, RMI.
4. Owing to the similarity of the equations describing flows with thermal and compositional density variations, cross-fertilization of ideas might bring new insights and research directions, e.g., with respect to the role of material properties or transition to turbulence in RTI and of layer asymmetries and scalings in vertical convection.
5. The mathematical validity of a set of conservation equations may not be guaranteed by its physical derivation. In particular, large gradients may develop due to nonlinear interactions, violating small parameter expansions. Such issues could be explored using accurate simulations with more general physical descriptions.
6. Turbulence models need to be explored that are formulated to be consistent with the inviscid scale decomposition criterion.

DISCLOSURE STATEMENT

The author is not aware of any biases that might be perceived as affecting the objectivity of this review.

ACKNOWLEDGMENTS

Los Alamos National Laboratory is operated by Triad National Security, LLC, for the National Nuclear Security Administration of the US Department of Energy (contract number 92689233218CNA000001). The author thanks J.R. Baltzer, Y. Tian, F.A. Jaberi, J.R. Ristorcelli, D. Aslangil, A. Banerjee, M.L. Wong, S.K. Lele, M.J. Andrews, R.A. Gore, K.P. Prestridge, H. Aluie, B. Nadiga, B.J. Olson, and A.W. Cook for fruitful collaborations and extensive discussions about variable-density turbulence as well as help with the figures.

LITERATURE CITED

Aglitskiy Y, Velikovich AL, Karasik M, Metzler N, Zalesak S, et al. 2014. Basic hydrodynamics of Richtmyer-Meshkov-type growth and oscillations in the inertial confinement fusion-relevant conditions. *Philos. Trans. R. Soc. Lond. A* 368:1739–68

Ahlers G, Araujo FF, Funfschilling D, Grossmann S, Lohse D. 2007. Non-Oberbeck-Boussinesq effects in gaseous Rayleigh-Bénard convection. *Phys. Rev. Lett.* 98:054501

Ahlers G, Brown E, Araujo FF, Funfschilling D, Grossmann S, Lohse D. 2006. Non-Oberbeck-Boussinesq effects in gaseous Rayleigh-Bénard convection. *J. Fluid Mech.* 569:409–45

Akula B, Ranjan D. 2016. Dynamics of buoyancy-driven flows at moderately high Atwood numbers. *J. Fluid Mech.* 795:313–55

Almagro A, García-Villalba M, Flores O. 2017. A numerical study of a variable-density low-speed turbulent mixing layer. *J. Fluid Mech.* 830:569–601

Almgren AS, Bell JB, Rendleman CA, Zingale M. 2006a. Low Mach number modeling of type Ia supernovae. I. Hydrodynamics. *Astrophys. J.* 637:922–36

Almgren AS, Bell JB, Rendleman CA, Zingale M. 2006b. Low Mach number modeling of type Ia supernovae. II. Energy evolution. *Astrophys. J.* 649:927

Aluie H. 2013. Scale decomposition in compressible turbulence. *Physica D* 24:54–65

Amielh M, Djeridane T, Anslemet F, Fulachier F. 1996. Velocity near-field of variable density turbulent jets. *Int. J. Heat Mass Transfer* 39:2149–64

Andreopoulos Y, Agui JH, Briassulis G. 2000. Shock wave–turbulence interactions. *Annu. Rev. Fluid Mech.* 32:309–45

Andrews MJ, Youngs DL, Livescu D, Wei T. 2014. Computational studies of two-dimensional Rayleigh-Taylor driven mixing for a tilted-rig. *ASME J. Fluids Eng.* 136:091212

Ashurst WT, Kerstein AR. 2005. One-dimensional turbulence: variable density formulation and application to mixing layers. *Phys. Fluids* 17:025107

Aslangil D, Livescu D, Banerjee A. 2017. *High-Atwood number effects on buoyancy-driven variable density homogeneous turbulence*. Paper presented at the 16th European Turbulence Conference, Stockholm, Sweden, Aug. 21–24

Attili A, Bisetti F. 2012. Statistics and scaling of turbulence in a spatially developing mixing layer at $\mathrm{Re}_\lambda = 250$. *Phys. Fluids* 24:035109

Balakumar BJ, Orlicz GC, Ristorcelli JR, Balasubramania S, Prestridge KP, Tomkins CD. 2012. Turbulent mixing in a Richtmyer–Meshkov fluid layer after reshock: velocity and density statistics. *J. Fluid Mech.* 696:67–93

Balasubramanian S, Orlicz GC, Prestridge KP, Balakumar BJ. 2012. Experimental study of initial condition dependence on Richtmyer-Meshkov instability in the presence of reshock. *Phys. Fluids* 24:034103

Baltzer JR, Livescu D. 2019. Low-speed turbulent shear-driven mixing layers with large thermal and compositional density variations. In *Modeling and Simulation of Turbulent Mixing and Reaction: For Power, Energy, and Flight*, ed. D Livescu, F Battaglia, P Givi. Singapore: Springer Nature

Banerjee A, Andrews MJ. Statistically steady measurements of Rayleigh–Taylor mixing in a gas channel. *Phys. Fluids* 18:035107

Banerjee A, Kraft WN, Andrews MJ. 2010. Detailed measurements of a statistically steady Rayleigh–Taylor mixing layer from small to high Atwood numbers. *J. Fluid Mech.* 659:127–90

Batchelor GK, Canuto VM, Chasnov JR. 1992. Homogeneous buoyancy-generated turbulence. *J. Fluid Mech.* 235:349–78

Beale JT, Kato T, Majda A. 1984. Remarks on the breakdown of smooth solutions for the 3-D Euler equations. *Commun. Math. Phys.* 94:61–66

Bird GA. 1961. The motion of a shock-wave through a region of non-uniform density. *J. Fluid Mech.* 11:180–86

Boffetta G, Mazzino A. 2017. Incompressible Rayleigh–Taylor turbulence. *Annu. Rev. Fluid Mech.* 49:119–43

Boukharfane R, Bouali Z, Mura A. 2018. Evolution of scalar and velocity dynamics in planar shock-turbulence interaction. *Shock Waves* 28:1117–41

Brouillette M. 2002. The Richtmyer–Meshkov instability. *Annu. Rev. Fluid Mech.* 34:445–68

Brown G. 1974. The entrainment and large structure in turbulent mixing layers. In *Proceedings of the 5th Australasian Conference on Hydraulics and Fluid Mechanics*, Vol. 1, ed. D Lindley, AJ Sutherland, pp. 352–59. Christchurch, N.Z.: Canterbury Univ.

Brown GL, Roshko A. 1974. On density effects and large structure in turbulent mixing layers. *J. Fluid Mech.* 64:775–816

Cabot W, Cook A. 2006. Reynolds number effects on Rayleigh–Taylor instability with possible implications for type-Ia supernovae. *Nat. Phys.* 2:562–68

Cabot W, Zhou Y. 2013. Statistical measurements of scaling and anisotropy of turbulent flows induced by Rayleigh–Taylor instability. *Phys. Fluids* 25:015107

Chandrasekhar S. 1981. *Hydrodynamic and Hydromagnetic Stability*. New York: Dover

Charonko JJ, Prestridge K. 2017. Variable density mixing in turbulent jets with coflow. *J. Fluid Mech.* 825:887–921

Chassaing P, Antonia RA, Anselmet F, Joly L, Sarkar S. 2002. *Variable Density Fluid Turbulence*. Dordrecht, Neth.: Springer Neth.

Chenoweth DR, Paolucci S. 1986. Natural convection in an enclosed vertical air layer with large horizontal temperature differences. *J. Fluid Mech.* 169:173–210

Chisnell R. 1955. The normal motion of a shock wave through a non-uniform one-dimensional medium. *Proc. R. Soc. Lond. A* 232:350–70
Chung D, Pullin DI. 2010. Direct numerical simulation and large-eddy simulation of stationary buoyancy-driven turbulence. *J. Fluid Mech.* 643:279–308
Cook AW, Cabot WH, Miller PL. 2004. The mixing transition in Rayleigh–Taylor instability. *J. Fluid Mech.* 511:333–62
Cook AW, Dimotakis PE. 2001. Transition stages of Rayleigh–Taylor instability between miscible fluids. *J. Fluid Mech.* 443:69–99
Day MS, Bell JB. 2000. Numerical simulation of laminar reacting flow with complex chemistry. *Combust. Theor. Model.* 4:535–56
de Lira CHR, Velikovich AL, Wouchuk JG. 2011. Analytical linear theory for the interaction of a planar shock wave with a two-or three-dimensional random isotropic density field. *Phys. Rev. E* 83:056320
Dimonte G, Schneider M. 2000. Density ratio dependence of Rayleigh-Taylor mixing for sustained and impulsive acceleration histories. *Phys. Fluids* 12:304–21
Dimonte G, Youngs DL, Wunsch S, Garasi C, Robinson A, et al. 2004. A comparative study of the turbulent Rayleigh-Taylor instability using high-resolution three-dimensional numerical simulations: the Alpha-Group collaboration. *Phys. Fluids* 16:1668–92
Dimotakis PE. 1984. Two-dimensional shear layer entrainment. *AIAA J.* 24:1791–96
Dimotakis PE. 2000. The mixing transition in turbulent flows. *J. Fluid Mech.* 409:69–98
Dimotakis PE. 2005. Turbulent mixing. *Annu. Rev. Fluid Mech.* 37:329–56
Donzis DA, Gibbon JD, Kerr RM, Gupta A, Pandit R, Vincenzi D. 2013. Vorticity moments in four numerical simulations of the 3D Navier–Stokes equations. *J. Fluid Mech.* 732:316–31
Eyink GL. 2005. Locality of turbulent cascades. *Physica D* 207:91–116
Freund JB, Lele SK, Moin P. 2000. Compressibility effects in a turbulent annular mixing layer. Part 1. Turbulence and growth rate. *J. Fluid Mech.* 421:229–67
Fusegi T, Hyun JM, Kuwahara K, Farouk B. 1990. A numerical study of three-dimensional natural convection in a differentially heated cubical enclosure. *Int. J. Heat Mass Transfer* 34:1543–57
Garnier E, Adams N, Sagaut P. 2009. *Large Eddy Simulation for Compressible Flows*. Dordrecht, Neth.: Springer Sci. Bus. Media
Gat I, Matheou G, Chung D, Dimotakis PE. 2017. Incompressible variable-density turbulence in an external acceleration field. *J. Fluid Mech.* 827:506–35
Gauthier S. 2017. Compressible Rayleigh–Taylor turbulent mixing layer between Newtonian miscible fluids. *J. Fluid Mech.* 830:211–56
Gerashchenko S, Prestridge K. 2015. Density and velocity statistics in variable density turbulent mixing. *J. Turbul.* 16:1011–35
Gibbon JD. 2015. High–low frequency slaving and regularity issues in the 3D Navier–Stokes equations. *IMA J. Appl. Math.* 812:308–20
Gibbon JD, Donzis DA, Kerr RM, Gupta A, Pandit R, Vincenzi D. 2014. Regimes of nonlinear depletion and regularity in the 3D Navier–Stokes equations. *Nonlinearity* 27:2605
Gilet C, Almgren AS, Bell JB, Nonaka A, Woosley SE, Zingale M. 2013. Low Mach number modeling of core convection in massive stars. *Astrophys. J.* 773:137
Givi P. 1989. Model-free simulations of turbulent reacting flows. *Progr. Energy Combust. Sci.* 15:1–107
Gray DD, Giorgini A. 1976. The validity of the Boussinesq approximation for liquids and gases. *Int. J. Heat Mass Transf.* 19:545–51
Griffond J. 2005. Linear interaction analysis applied to a mixture of two perfect gases. *Phys. Fluids* 17:086101
Griffond J, Soulard O. 2012. Evolution of axisymmetric weakly turbulent mixtures interacting with shock or rarefaction waves. *Phys. Fluids* 24:115108
Griffond J, Soulard O, Souffland D. 2010. A turbulent mixing Reynolds stress model fitted to match linear interaction analysis prediction. *Phys. Scr.* 2010:014059
Hesselink L, Sturtevant B. 1988. Propagation of weak shocks through a random medium. *J. Fluid Mech.* 196:513–53
Hill DJ, Pantano C, Pullin DI. 2006. Large-eddy simulation and multiscale modelling of a Richtmyer–Meshkov instability with reshock. *J. Fluid Mech.* 557:29–61

Hughes GO, Griffiths RW. 2008. Horizontal convection. *Annu. Rev. Fluid Mech.* 40:185–208
Jamme S, Cazalbou JB, Torres F, Chassaing P. 2002. Direct numerical simulation of the interaction between a shock wave and various types of isotropic turbulence. *Flow Turbul. Combust.* 68:227–68
Joseph DD. 1990. Fluid dynamics of two miscible liquids with diffusion and gradient stresses. *Eur. J. Mech. B* 6:565–96
Khokhlov AM, Oran ES, Thomas GO. 1999. Numerical simulation of deflagration-to-detonation transition: the role of shock–flame interactions in turbulent flames. *Combust. Flame* 117:323–39
Koochesfahani MM, Dimotakis PE. 1986. Mixing and chemical reactions in a turbulent liquid mixing layer. *J. Fluid Mech.* 170:83–112
Kovasznay LSG. 1953. Turbulence in supersonic flow. *J. Aeronaut. Sci.* 20:657–74
Larsson J, Bermejo-Moreno I, Lele SK. 2013. Reynolds- and Mach-number effects in canonical shock–turbulence interaction. *J. Fluid Mech.* 717:293–321
Larsson J, Lele SK. 2009. Direct numerical simulation of canonical shock/turbulence interaction. *Phys. Fluids* 21:126101
Lee S, Lele SK, Moin P. 1993. Direct numerical simulation of isotropic turbulence interacting with a weak shock wave. *J. Fluid Mech.* 251:533–62
Livescu D. 2013. Numerical simulations of two-fluid turbulent mixing at large density ratios and applications to the Rayleigh–Taylor instability. *Philos. Trans. R. Soc. A* 371:20120185
Livescu D, Canada C, Kanov K, Burns R, IDIES Staff, Pulido J. 2014. *Homogeneous buoyancy driven turbulence data set*. Data Set README, Johns Hopkins Turbul. Databases, Johns Hopkins Univ., Baltimore, MD. **http://turbulence.pha.jhu.edu/docs/README-HBDT.pdf**
Livescu D, Ristorcelli JR. 2007. Buoyancy-driven variable-density turbulence. *J. Fluid Mech.* 591:43–71
Livescu D, Ristorcelli JR. 2008. Variable-density mixing in buoyancy-driven turbulence. *J. Fluid Mech.* 605:145–80
Livescu D, Ristorcelli JR. 2009. Mixing asymmetry in variable-density turbulence. In *Advances in Turbulence XII: Proceedings of the 12th EUROMECH European Turbulence Conference, September 7–10, 2009, Marburg, Germany*, ed. B Eckhardt, pp. 545–48. Berlin: Springer
Livescu D, Ristorcelli JR, Gore RA, Dean SH, Cabot WH, Cook AW. 2009. High–Reynolds number Rayleigh–Taylor turbulence. *J. Turbul.* 10:N13
Livescu D, Ristorcelli JR, Petersen MR, Gore RA. 2010. New phenomena in variable–density Rayleigh–Taylor turbulence. *Phys. Scr.* 2010:014015
Livescu D, Ryu J. 2016. Vorticity dynamics after the shock–turbulence interaction. *Shock Waves* 26:241–51
Livescu D, Wei T, Petersen MR. 2011. Direct numerical simulations of Rayleigh-Taylor instability. *J. Phys. Conf. Ser.* 318:082007
Lohse D, Xia KQ. 2010. Small-scale properties of turbulent Rayleigh-Bénard convection. *Annu. Rev. Fluid Mech.* 42:335–64
Lombardini M, Hill DJ, Pullin DI, Meiron DI. 2011. Atwood ratio dependence of Richtmyer–Meshkov flows under reshock conditions using large-eddy simulations. *J. Fluid Mech.* 670:439–80
Lombardini M, Pullin DI, Meiron DI. 2012. Transition to turbulence in shock-driven mixing: a Mach number study. *J. Fluid Mech.* 690:203–26
Lombardini M, Pullin DI, Meiron DI. 2014a. Turbulent mixing driven by spherical implosions. Part 1. Flow description and mixing-layer growth. *J. Fluid Mech.* 748:85–112
Lombardini M, Pullin DI, Meiron DI. 2014b. Turbulent mixing driven by spherical implosions. Part 2. Turbulence statistics. *J. Fluid Mech.* 748:113–42
Mahesh K, Lee S, Lele SK, Moin P. 1995. The interaction of an isotropic field of acoustic waves with a shock wave. *J. Fluid Mech.* 300:383–407
Mahesh K, Lele SK, Moin P. 1997. The influence of entropy fluctuations on the interaction of turbulence with a shock wave. *J. Fluid Mech.* 334:353–79
Majda A, Sethian J. 1985. The derivation and numerical solution of the equations for zero Mach number combustion. *Combust. Sci. Tech.* 42:185–205
McMurtry PA, Jou WH, Riley JJ, Metcalfe RW. 1986. Direct numerical simulations of a reacting mixing layer with chemical heat release. *AIAA J.* 24:962–70

Miller RS, Harstad KG, Bellan J. 2001. Direct numerical simulation of supercritical fluid mixing layers applied to heptane-nitrogen. *J. Fluid Mech.* 436:1–39

Mohaghar M, Carter J, Musci B, Reilly D, McFarland J, Ranjan D. 2017. Evaluation of turbulent mixing transition in a shock-driven variable-density flow. *J. Fluid Mech.* 831:779–825

Moore FK. 1954. *Unsteady oblique interaction of a shock wave with a plane disturbance*. Tech. Rep. 1165, Natl. Advis. Comm. Aeronaut., Lewis Flight Propuls. Lab., Cleveland, OH

Motheau E, Abraham J. 2016. A high-order numerical algorithm for DNS of low-Mach-number reactive flows with detailed chemistry and quasi-spectral accuracy. *J. Comput. Phys.* 313:430–54

Nicoud F. 2000. Conservative high-order finite-difference schemes for low-Mach number flows. *J. Comp. Phys.* 158:71–97

Nonaka A, Almgren AS, Bell JB, Lijewski MJ, Malone CM, Zingale M. 2010. MAESTRO: An adaptive low Mach number hydrodynamics algorithm for stellar flows. *Astrophys. J. Suppl.* 188:358

O'Brien J, Urzay J, Ihme M, Moin P, Saghafian A. 2014. Subgrid-scale backscatter in reacting and inert supersonic hydrogen air turbulent mixing layers. *J. Fluid Mech.* 743:554–84

Olson BJ, Larsson J, Lele SK, Cook AW. 2011. Nonlinear effects in the combined Rayleigh-Taylor/Kelvin-Helmholtz instability. *Phys. Fluids* 23:114107

Orlicz GC, Balasubramanian S, Vorobieff P, Prestridge KP. 2015. Mixing transition in a shocked variable-density flow. *Phys. Fluids* 27:114102

Pantano C, Sarkar S. 2002. A study of compressibility effects in the high-speed turbulent shear layer using direct simulation. *J. Fluid Mech.* 451:329–71

Paolucci S, Chenoweth DR. 1989. Transition to chaos in a differentially heated vertical cavity. *J. Fluid Mech.* 201:379–410

Patel A, Boersma BJ, Pecnik R. 2016. The influence of near-wall density and viscosity gradients on turbulence in channel flows. *J. Fluid Mech.* 809:793–820

Pember RP, Howell LH, Bell JB, Collela P, Cruthfield WY, et al. 1998. An adaptive projection method for unsteady, low Mach number combustion. *Combust. Sci. Tech.* 140:123–68

Poggi F, Thorembey MH, Rodriguez G. 1998. Velocity measurements in turbulent gaseous mixtures induced by Richtmyer–Meshkov instability. *Phys. Fluids* 10:2698–700

Prestridge KP. 2018. Experimental adventures in variable-density mixing. *Phys. Rev. Fluids* 3:110501

Quadros R, Sinha K, Larsson J. 2016. Turbulent energy flux generated by shock/homogeneous-turbulence interaction. *J. Fluid Mech.* 796:113–57

Rajagopal KR, Ruzicka M, Srinivasa AR. 1996. On the Oberbeck–Boussinesq approximation. *Math. Model. Meth. Appl.* 6:1157–67

Ramaprabhu P, Dimonte G, Andrews MJ. 2005. A numerical study of the influence of initial perturbations on the turbulent Rayleigh–Taylor instability. *J. Fluid Mech.* 536:285–319

Ramaprabhu P, Dimonte G, Young Y, Calder AC, Fryxell B. 2006. Limits of the potential flow approach to the single-mode Rayleigh-Taylor problem. *Phys. Rev. E* 74:066308

Ranjan D, Oakley J, Bonazza R. 2011. Shock-bubble interactions. *Annu. Rev. Fluid Mech.* 43:117–40

Rao P, Caulfield CP, Gibbon JD. 2017. Nonlinear effects in buoyancy-driven variable-density turbulence. *J. Fluid Mech.* 810:362–77

Reese DT, Ames AM, Noble CD, Oakley JG, Rothamer DA, Bonazza R. 2018. Simultaneous direct measurements of concentration and velocity in the Richtmyer–Meshkov instability. *J. Fluid Mech.* 849:541–75

Rehm RG, Baum HR. 1978. The equations of motion of thermally driven buoyant flows. *J. Res. Natl. Bur. Stand.* 83:297–308

Remington BA, Park HS, Casey DT, Cavallo RM, Clark DS, et al. 2019. Rayleigh–Taylor instabilities in high-energy density settings on the National Ignition Facility. *PNAS* 116:18233–38

Ribner HS. 1954. *Convection of a pattern of vorticity through a shock wave*. Tech. Rep. 1164, Natl. Advis. Comm. Aeronaut., Lewis Flight Propuls. Lab., Cleveland, OH

Ristorcelli J, Clark T. 2004. Rayleigh–Taylor turbulence: self-similar analysis and direct numerical simulations. *J. Fluid Mech.* 507:213–53

Roberts MS, Jacobs JW. 2016. The effects of forced small-wavelength, finite-bandwidth initial perturbations and miscibility on the turbulent Rayleigh–Taylor instability. *J. Fluid Mech.* 787:50–83

Ryu J, Livescu D. 2014. Turbulence structure behind the shock in canonical shock-vortical turbulence interaction. *J. Fluid Mech.* 756:R1

Safta C, Ray J, Najm HN. 2010. A high-order low-Mach number AMR construction for chemically reacting flows. *J. Comput. Phys.* 229:9299–322

Sagaut P, Cambon C. 2018. *Homogeneous Turbulence Dynamics*. Cham, Switz.: Springer. 2nd ed.

Sandoval D. 1995. *The dynamics of variable-density turbulence*. Ph.D. Thesis, Univ. Wash., Seattle, WA

Schwarzkopf JD, Livescu D, Baltzer JR, Gore RA, Ristorcelli JR. 2016. A two length-scale turbulence model for single-phase multi-fluid mixing. *Flow Turbul. Combust.* 96:1–43

Sethuraman YPM, Sinha K, Larsson J. 2018. Thermodynamic fluctuations in canonical shock–turbulence interaction: effect of shock strength. *Theor. Comput. Fluid Dyn.* 32:629–54

Sharp D. 1984. An overview of Rayleigh-Taylor instability. *Physica D* 12:3–18

Soukhomlinov VS, Kolosov VY, Sheverev VA, Ötügen MV. 2002. Formation and propagation of a shock wave in a gas with temperature gradients. *J. Fluid Mech.* 473:245–64

Swisher NC, Kuranz CC, Arnett D, Hurricane O, Remington BA, et al. 2015. Rayleigh-Taylor mixing in supernova experiments. *Phys. Plasmas* 22:102707

Thornber B, Drikakis D, Youngs DL, Williams RJR. 2010. The influence of initial conditions on turbulent mixing due to Richtmyer–Meshkov instability. *J. Fluid Mech.* 654:99–139

Thornber B, Drikakis D, Youngs DL, Williams RJR. 2011. Growth of a Richtmyer–Meshkov turbulent layer after reshock. *Phys. Fluids* 23:095107

Thornber B, Griffond J, Poujade O, Attal A, Varshochi H, et al. 2017. Late-time growth rate, mixing, and anisotropy in the multimode narrowband Richtmyer–Meshkov instability: the θ-group collaboration. *Phys. Fluids* 29:105107

Thornber B, Zhou Y. 2015. Numerical simulations of the two-dimensional multimode Richtmyer–Meshkov instability. *Phys. Plasmas* 22:032309

Tian Y, Jaberi FA, Li Z, Livescu D. 2017. Numerical study of variable density turbulence interaction with a normal shock wave. *J. Fluid Mech.* 829:551–88

Tian Y, Jaberi FA, Livescu D. 2019a. Density effects on the post-shock turbulence structure and dynamics. *J. Fluid Mech.* 880:935–68

Tian Y, Jaberi FA, Livescu D. 2019b. Shock propagation in media with non-uniform density. In *31st International Symposium on Shock Waves I*, ed. A Sasoh, T Aoki, M Katayama, pp. 1167–75. Cham, Switz.: Springer

Tomkins C, Kumar S, Orlicz GC, Prestridge KP. 2008. An experimental investigation of mixing mechanisms in shock-accelerated flow. *J. Fluid Mech.* 611:131–50

Tritschler VK, Olson BJ, Lele SK, Hickel S, Hu XY, Adams NA. 2014a. On the Richtmyer–Meshkov instability evolving from a deterministic multimode planar interface. *J. Fluid Mech.* 755:429–62

Tritschler VK, Zubel M, Hickel S, Adams NA. 2014b. Evolution of length scales and statistics of Richtmyer-Meshkov instability from direct numerical simulations. *Phys. Rev. E* 90:063001

Villermaux E. 2019. Mixing versus stirring. *Annu. Rev. Fluid Mech.* 51:245–73

Vreman AW, Sandham ND, Luo KH. 1996. Compressible mixing layer growth rate and turbulence characteristics. *J. Fluid Mech.* 320:235–58

Wang Q, Xia SN, Yan R, Sun DJ, Wan ZH. 2019. Non-Oberbeck-Boussinesq effects due to large temperature differences in a differentially heated square cavity filled with air. *Int. J. Heat Mass Transfer* 128:479–91

Weber CR, Cook AW, Bonazza R. 2013. Growth rate of a shocked mixing layer with known initial perturbations. *J. Fluid Mech.* 725:372–401

Weber CR, Haehn NS, Oakley JG, Rothamer DA, Bonazza R. 2014. An experimental investigation of the turbulent mixing transition in the Richtmyer–Meshkov instability. *J. Fluid Mech.* 748:457–87

Wei T, Livescu D. 2012. Late-time quadratic growth in single-mode Rayleigh-Taylor instability. *Phys. Rev. E* 86:046405

Whitham G. 1958. On the propagation of shock waves through regions of non-uniform area or flow. *J. Fluid Mech.* 4:337–60

Williams F. 1985. *Combustion Theory*. Cambridge, MA: Perseus

Wong ML, Livescu D, Lele SK. 2019. High-resolution Navier-Stokes simulations of Richtmyer-Meshkov instability with re-shock. *Phys. Rev. Fluids* 4:104609

Youngs D. 1984. Numerical simulation of turbulent mixing by Rayleigh–Taylor instability. *Physica D* 12:32–44

Youngs D. 1994. Numerical simulation of mixing by Rayleigh–Taylor and Richtmeyer–Meshkov instabilities. *Laser Part. Beams* 12:725–50

Youngs DL. 2013. The density ratio dependence of self-similar Rayleigh–Taylor mixing. *Philos. Trans. R. Soc. A* 371:20120173

Youngs DL. 2017. Rayleigh–Taylor mixing: direct numerical simulation and implicit large eddy simulation. *Phys. Scr.* 92:074006

Zabusky NJ. 1999. Vortex paradigm for accelerated inhomogeneous flows: visiometrics for the Rayleigh-Taylor and Richtmyer-Meshkov environments. *Annu. Rev. Fluid Mech.* 31:495–536

Zhao D, Aluie H. 2018. Inviscid criterion for decomposing scales. *Phys. Rev. Fluids* 3:054603

Zhou Y. 2017a. Rayleigh–Taylor and Richtmyer–Meshkov instability induced flow, turbulence, and mixing. I. *Phys. Rep.* 720–22:1–136

Zhou Y. 2017b. Rayleigh–Taylor and Richtmyer–Meshkov instability induced flow, turbulence, and mixing. II. *Phys. Rep.* 723–25:1–160

Zhou Y, Cabot WH, Thornber B. 2016. Asymptotic behavior of the mixed-mass in Rayleigh–Taylor and Richtmyer–Meshkov induced flows. *Phys. Plasmas* 23:052712

Zingale M, Almgren AS, Bell JB, Nonaka A, Woosley SE. 2009. Low Mach number modeling of type Ia supernovae. IV. White dwarf convection. *Astrophys. J.* 704:196–210

Zingale M, Malone CM, Nonaka A, Almgren AS, Bell JB. 2015. Comparisons of two- and three-dimensional convection in type I X-ray bursts. *Astrophys. J.* 807:60

Annual Review of
Fluid Mechanics

Volume 52, 2020

Contents

Indexes

Errata

An online log of corrections to *Annual Review of Fluid Mechanics* articles may be found at http://www.annualreviews.org/errata/fluid